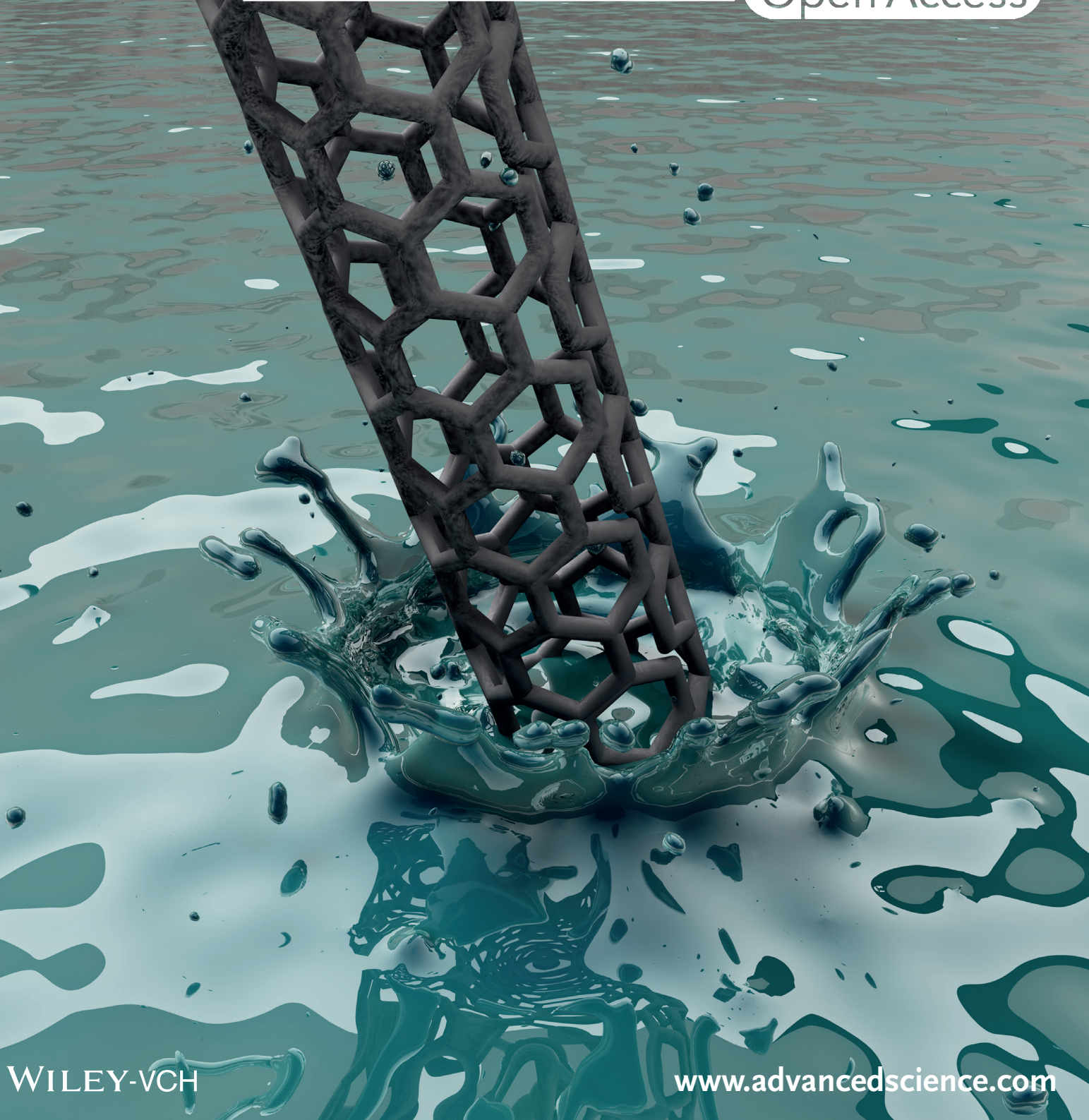


Vol. 5 • No. 7 • July 2018

# ADVANCED SCIENCE

Open Access



# Intragranular Dispersion of Carbon Nanotubes Comprehensively Improves Aluminum Alloys

Kang Pyo So, Akihiro Kushima, Jong Gil Park, Xiaohui Liu, Dong Hoon Keum, Hye Yun Jeong, Fei Yao, Soo Hyun Joo, Hyoung Seop Kim, Hwanuk Kim, Ju Li,\* and Young Hee Lee\*

The room-temperature tensile strength, toughness, and high-temperature creep strength of 2000, 6000, and 7000 series aluminum alloys can be improved significantly by dispersing up to 1 wt% carbon nanotubes (CNTs) into the alloys without sacrificing tensile ductility, electrical conductivity, or thermal conductivity. CNTs act like forest dislocations, except mobile dislocations cannot annihilate with them. Dislocations cannot climb over 1D CNTs unlike 0D dispersoids/precipitates. Also, unlike 2D grain boundaries, even if some debonding happens along 1D CNT/alloy interface, it will be less damaging because fracture intrinsically favors 2D percolating flaws. Good intragranular dispersion of these 1D strengtheners is critical for comprehensive enhancement of composite properties, which entails change of wetting properties and encapsulation of CNTs inside Al grains via surface diffusion-driven cold welding. In situ transmission electron microscopy demonstrates liquid-like envelopment of CNTs into Al nanoparticles by cold welding.

because aluminum has about half the melting point of iron (933.5 K vs 1811 K) and becomes very soft at 500 K or so. This is a mature market, so property changes at a few to tens of percent could change alloy choices within the family, if (a) the increase in cost is not very dramatic and (b) not just one single property, but a comprehensive list of properties are improved. In light of (a) and (b), we will examine the practice of dispersing carbon nanotubes (CNTs) into aluminum alloys. In the previous paper,<sup>[1]</sup> we have dispersed CNTs into pure aluminum at ton-scale and summarized the effects on room-temperature (RT) properties by a “Taylor-dispersion hardening” model. The gist is that well-dispersed CNTs act like forest dislocations. It can harden the metal pretty much like stored dislocation line density in the traditional Taylor work-hardening model, giving rise

to a nonlocal latent hardening of the metal matrix as well as still acting like a composite filler and transmitting load directly as in the traditional composite shear-lag model. Because mass-produced multiwalled carbon nanotubes (MWCNT) cost  $\approx \$10^2 \text{ kg}^{-1}$  nowadays, dispersing  $\approx 1 \text{ wt\%}$  MWCNT into Al matrix would only double the alloy cost which is considered to be a reasonable economic boundary today. Depending on the dispersion

## 1. Introduction

Aluminum alloys command a \$100+ billion/year world market. The chief advantages of aluminum alloys compared with steels are the higher specific strength, electrical and thermal conductivities, and corrosion resistance. The disadvantages are the cost and high-temperature capabilities

Dr. K. P. So, Prof. A. Kushima, Prof. X. Liu, Prof. J. Li  
 Department of Nuclear Science and Engineering  
 and Department of Materials Science and Engineering  
 Massachusetts Institute of Technology  
 Cambridge, MA 02139, USA  
 E-mail: liju@mit.edu

Prof. A. Kushima  
 Advanced Materials Processing and Analysis Center  
 University of Central Florida  
 Orlando, FL 32816, USA

 The ORCID identification number(s) for the author(s) of this article can be found under <https://doi.org/10.1002/advs.201800115>.

© 2018 The Authors. Published by WILEY-VCH Verlag GmbH & Co. KGaA, Weinheim. This is an open access article under the terms of the Creative Commons Attribution License, which permits use, distribution and reproduction in any medium, provided the original work is properly cited.

DOI: [10.1002/advs.201800115](https://doi.org/10.1002/advs.201800115)

J. G. Park, D. H. Keum, Dr. H. Y. Jeong, Prof. F. Yao, Prof. Y. H. Lee  
 IBS Center for Integrated Nanostructure Physics  
 Institute for Basic Science (IBS)  
 Sungkyunkwan University  
 Suwon 440-746, Republic of Korea  
 E-mail: leeyoung@skku.edu

Prof. X. Liu  
 School of Materials Science and Engineering  
 Shanghai Jiao Tong University  
 Shanghai 200240, China

Prof. S. H. Joo, Prof. H. S. Kim  
 Department of Materials Science and Engineering  
 Pohang University of Science and Technology  
 Pohang 790-784, Republic of Korea

Dr. H. Kim  
 Division of Electron Microscopic Research  
 Korea Basic Science Institute  
 113 Gwahangno, Yuseong-Gu, Daejeon 305-333, Republic of Korea

**Table 1.** Mechanical properties of Al alloy-CNTs composites.

Matrix	CNTs [wt%]	Tensile strength [MPa] (relative change (%))	Yield strength [MPa] (relative change (%))	Young's modulus [GPa] (relative change (%))	Fracture strain [%] (relative change (%))
Pure Al	1	201( $\pm 0.58$ )(51%)	100( $\pm 16$ )(30%)	80( $\pm 0.18$ )(16.5%)	21( $\pm 2.2$ )(-11%)
6000 series	1	227( $\pm 3.6$ )(43%)	143( $\pm 4.2$ )(32%)	–	9.6( $\pm 1.8$ )(-10%)
7000 series	1	264( $\pm 1.5$ )(48%)	–	–	15( $\pm 0.6$ )(-6%)
2000 series	1	295( $\pm 13.5$ )(45%)	192( $\pm 7.5$ )(59%)	–	5.9( $\pm 1.4$ )(-15%)
AlCu/AlSiMg	0.5	429( $\pm 6.4$ )(13%)	383( $\pm 7$ )(16%)	141( $\pm 1.6$ )(0%)	4.75( $\pm 0.5$ )(-36%)
AlCu/AlSiMg (HPT) <sup>a)</sup>	1	612(20%)	517(8.2%)	70(-4%)	3.14(8.3%)
Dual phase steel <sup>b)</sup>	0	500	300	–	30–34

<sup>a)</sup>High-pressure torsion (HPT); <sup>b)</sup>This steel is usually used for automobile body ([www.worldautosteel.org](http://www.worldautosteel.org)).

and the MWCNT diameter, 1 wt% (equivalent to about 2 vol%) MWCNT would give rise to a dispersed line length density  $\rho_{\text{CNT}} = 10^{13}\text{--}10^{15} \text{ m}^{-2}$ . In the present paper, we first show that intragranular MWCNT dispersion is possible in various aluminum alloys (2000, 6000, and 7000 series), and significant improvement in room-temperature tensile strength can be achieved on top of the well-known precipitate strengthening mechanism in Al alloys without adverse effect on tensile toughness (Table 1). We then prove that the electrical and thermal conductivities are also slightly improved, which is the first in this field. Then, we show that because mobile dislocations can hardly climb over 1D nanodispersoids (in contrast, they can more easily climb over 0D precipitates, by vacancy flux aided nonconservative dislocation motion), the creep strength of Al alloys is significantly enhanced with its high-temperature capability raised by 50–100 K, which could be significant for some applications. Lastly, we discuss the underlying reason for the comprehensive enhancements, the key being the good intragranular dispersion we have obtained, that is, the CNTs do not sit only at the grain boundaries (GBs) even though initially that was where they were at, but are also well distributed inside the grains, matching the “Taylor-dispersion hardening” picture as the bulk dislocation line density is also distributed inside grains. This was in turn rationalized by “cold welding” and rapid surface diffusion of Al atoms in vacuum-environment mechanical ball milling, which buried the MWCNTs inside the master alloy particles. This cold welding and burying process was revealed by *in situ* transmission electron microscopy (TEM) experiments under similar vacuum conditions. Our way of producing master alloy and dispersing them are thus key for the comprehensive superiority of the properties over other methods of making metal + CNT nanocomposites.

## 2. Materials and Methods

Good dispersion of CNTs was achieved by the processing flow chart shown in Figure 1. A key intermediate product is the master alloy, a solid powder consisting of 0.1–5 wt% CNTs. Depending on the postmaster consolidation process (which all involves temperature higher than RT) such as melt blending

or sintering, premaster surface modification may be required to enhance the wetting and the interfacial strength, that entails coating SiC or  $\text{Al}_2\text{O}_3$  on CNT by thermal decomposition<sup>[2]</sup> and microwave treatment (Movie S1, Supporting Information). After the surface modification, we unravel the tangled MWCNTs by a high-speed blade mixer, which split the clusters into single strands of CNT on the surface of Al particles. The declustered CNTs were then buried inside the Al particles using a planetary ball mill under vacuum. As a consequence of the cold welding to be detailed later, CNTs are encapsulated

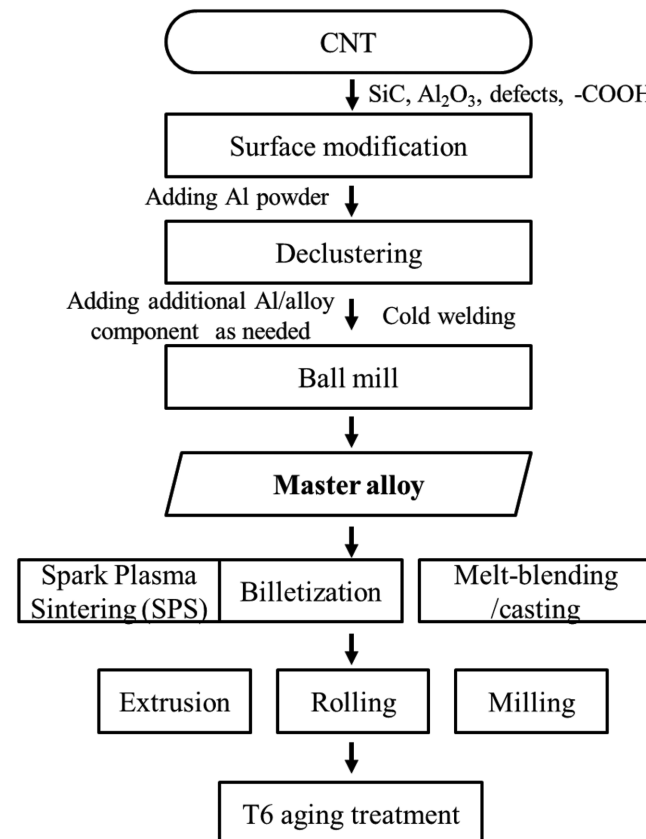


**Figure 1.** Flow chart of the Al/CNT fabrication process.

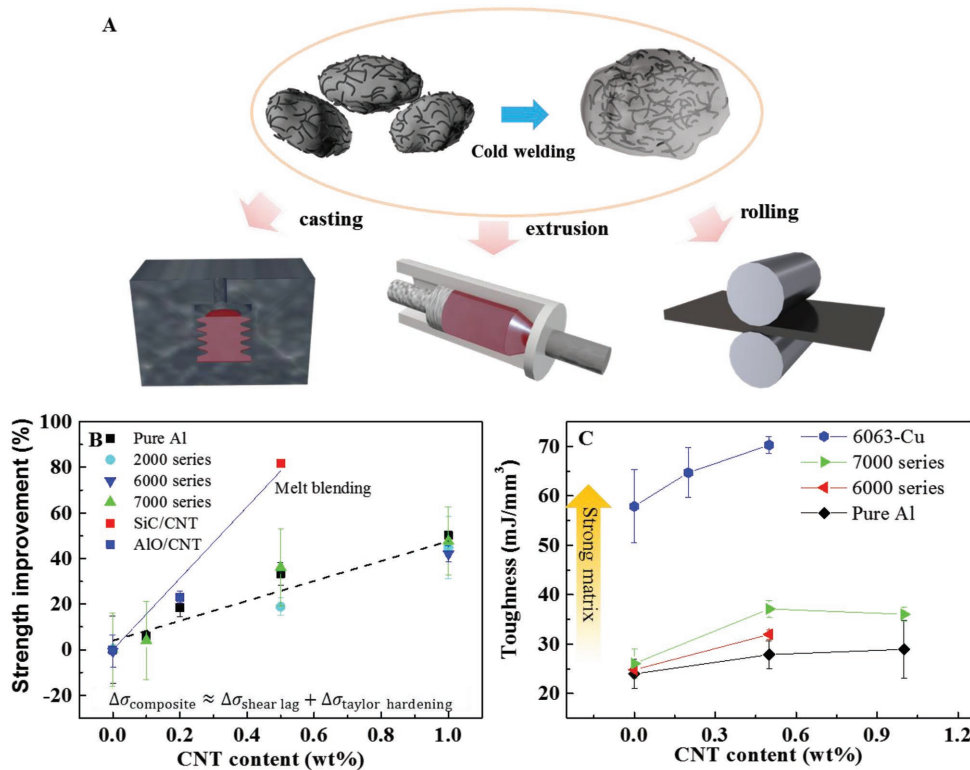


**Figure 2.** Schematic diagram of the fabrication process of Al + CNT and the mechanical properties. A) Schematic diagram of the declustering of CNT and cold welding. B) Strength improvement from the CNT in a different type of Al alloy and different fabrication methods. The SiC coated CNT was introduced for the melt casting method (red square). Other alloy samples were made using extrusion. C) toughness enhancement of Al alloys at various CNT concentrations.

inside Al grains, creating the master alloy (Figure 2A). The master alloy can then be further processed by spark plasma sintering (SPS), billetization or melting process/casting to create bulk specimen. SPS consolidated the granules and formed the interfacial Al–C covalent bonds. For the melt process, we decorated thin SiC layer on the surface of the CNT to improve the wetting to molten Al.<sup>[2]</sup> 5 wt% SiC/CNTs of the master alloy subsequently dissolved into molten Al alloy to become 0.5 wt% CNT (Movie S2, Supporting Information). The consolidated Al + CNT was further shaped by milling, extrusion, and rolling (detailed experimental parameters are described in Table S1, Supporting Information). Previously, we have studied pure Al + CNT.<sup>[1]</sup> To see the influence of CNT on alloys in this work, we introduced alloying elements during RT ball milling (mechanical alloying, MA) in Ar. After shaping (extrusion, rolling, and milling), all the alloy composites were subjected to T6 tempering including solution heat treatment and aging treatment, before the mechanical properties were measured.

From our measurements, regardless of the matrix composition and original mechanical properties, the dispersion of CNT in various Al alloys can improve the strength (after extrusion) by 40–50% at 1 wt% CNT (black dash in Figure 2B). Therefore, adding a small amount of CNTs strengthens the materials on the top of existing precipitation hardening. The absolute mechanical properties of different Al alloys are shown in Table 1. The strength increases more after Al<sub>2</sub>O<sub>3</sub> or SiC

surface modification on CNT. ≈80% strength improvement is achieved at 0.5 wt% after melt blending of SiC/CNT (red dot in Figure 1B). SiC has better wettability to Al than carbon, hence it significantly improves the wetting of CNT to molten Al, improving the interfacial bonding and nanoscale dispersion.

### 3. Results

With regard to ductility, although the formability range is slightly reduced, the nonuniform elongation (postnecking) increased, resulting in nearly unchanged tensile strain to failure  $\varepsilon_f$ . The toughness,  $\int_0^{\varepsilon_f} \sigma d\varepsilon$ , increases significantly as the CNT fraction approaches 1 wt% (Figure 2C). The dispersion of CNT significantly increases the absolute toughness of various Al alloys, even in complex multicomponent alloys such as Al–Cu precipitation on the top of A–Si–Mg alloy system, which enables one to measure the highest tensile toughness (Figure 2C, blue line 6063-Cu). Beyond 1 wt%, the toughness of some composites starts to drop even though the strength continues to increase. This should be because the critical length-scale for fracture is reached due to more and more severe CNT agglomeration with increasing CNT fraction.<sup>[3]</sup>

Electrical conductivity increases with up to 0.5 wt% CNTs, then gradually decreases (Figure 3A). To the best of our knowledge, no report has shown electrical conductivity

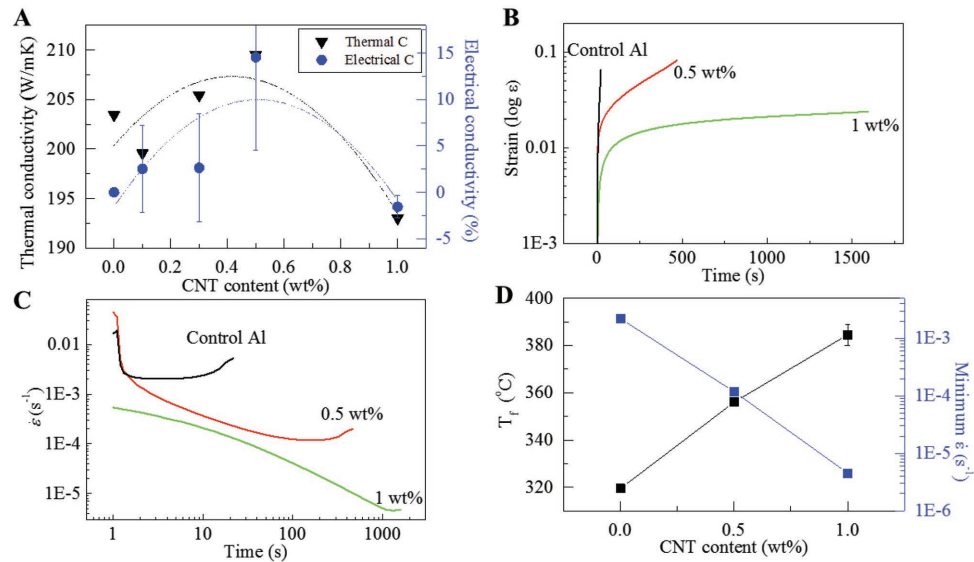


**Figure 3.** Electrical and thermal properties. A) Thermal conductivity and enhancement of electrical conductivities by adding CNT. B) Strain versus time and C)  $d\dot{\epsilon}/dt$  at different CNT contents under 300 °C, 70 MPa. D) Fractured temperature ( $T_f$ ) and minimum strain rate of Al + CNT composite.

improvement by adding carbon nanotubes in metals.<sup>[4,5]</sup> Although CNTs with superior electron mobility provides excellent electron transport channels, incoherent interface, and the Schottky barrier between CNT and Al (reported to be  $\approx 0.2$  eV<sup>[6]</sup>) are obstacles. However, good dispersion of CNT inside Al grain enhances electrical transport intra/inter-grains. The intimate contact between CNT and Al contributes to lowering the electron transport barrier. As a consequence, CNTs addition into Al slightly increases the electrical conductivity even though they increase mechanical strength. Likewise, Al alloys from the melt processing also show decreased sheet resistance with CNT additions (Figure S7, Supporting Information).<sup>[7]</sup> The thermal conductivity has a similar trend with the electrical conductivity. A few reports have shown that the thermal conductivity increases with up to 0.5 wt% of CNTs,<sup>[8,9]</sup> similar to our results.

It is conceptually intriguing to compare metal + CNT with other strategies of nanostrengthening, such as oxide-dispersed strengthened steels, and grain-boundary strengthened nanocrystalline metals. The unique feature of CNT is that it is 1D, which differs from 0D and 2D strengtheners. At high temperatures, a small amount of diffusion would allow dislocations to climb over 0D dispersoids/precipitates. But they would find it nearly impossible to climb over 1D CNTs that cross its path which have an aspect ratio as long as  $10^3$ . And unlike 1D forest dislocations which can be annihilated by dislocation reactions (recovery) and recrystallization, the 1D CNTs cannot be annihilated this way. They also do not coarsen like the grains do, since CNTs are not required to form a percolating network like the GBs, and there is also no significant thermodynamic driving force for CNT dispersion to coarsen like the grains when there is good wetting with metal. Thus, we expect the metal + CNT to have superior high-temperature creep strength than corresponding 0D strengthened alloys. Also, fracture favors percolating, 2D flaws because elastic fracture mechanics prefers planar cracks (oblate over prolate), so grain-boundary

strengthening, although highly effective at RT as shown by the Hall–Petch relation, also tends to embrittle the material macroscopically due to the extreme-value statistics nature of fracture. Furthermore, at high-temperature, grain boundary diffusion can greatly accelerate creep.

To evaluate the high-temperature creep strength, we measured the creep strain rate of Al + CNT at 300 °C (Figure 3B) or 573.15 K. As is well known, aluminum melts at  $T_M = 933.5$  K and usually becomes very soft above  $T_M/2$ . The strain rate was measured at 300 °C using dynamic mechanical analyzer (DMA) under 70 MPa engineering stress (dead load) for all samples. DMA requires very small sample (only few milligram) quantity and size and has good sensitivity in applying accurate force (10  $\mu\text{N}$ ) and temperature ( $\pm 0.1$  °C). It detects a very small range of displacements (1 nm). Thus, it is very efficient in evaluating creep properties. The measurement time is only a few minutes to hours. The pulling direction is aligned with the CNTs in the thin film geometry, which afford more effective pinning of dislocations climbing in transverse directions. The creep strain rate  $\dot{\epsilon}$  decreases by three orders of magnitude by adding 1 wt% (Figure 3C). The strain rate of pure Al + 1 wt% CNT in stage II is  $\approx 10^{-6}$   $\text{s}^{-1}$  at 300 °C and 70 MPa, similar to the reported  $\approx 20$  vol% SiC whisker/Al6063.<sup>[10]</sup>

Also, the creep fracturing of the specimen at high temperatures was measured using standard testing equipment (Applied Test Systems, Inc.) calibrated by American Society for Testing and Materials (ASTM) E4 with a dead load that corresponds to 50% of the RT yield strength of this material. The temperature was measured by welding two k-type thermocouples on the both ends of grip holder for accurate temperature estimation. The 300 mm length of the heater is big enough to cover the entire sample (50 mm) including grip holders. We use the linear variable differential transformer as an extensometer to measure the displacement when the temperature increases. The control pure Al creeps as the temperature rises at 100 °C  $\text{h}^{-1}$  and is fractured at 320 °C (Figure S6, Supporting Information).

In contrast, the 0.5 and 1 wt% CNT + Al showed reduced creep rate and fractured at significantly higher temperatures. The creep fracture temperature ( $T_f$ ) increases linearly with CNT addition (Figure 3D). The high-temperature ability is almost enhanced by 70 °C with 1 wt% CNT dispersion, which is very significant ( $0.08T_M$ ) in both relative and absolute terms. It means the range of applications of aluminum alloys may be significantly expanded.

#### 4. Discussion

Metal + CNT composites have been extensively studied during the last two decades, but most efforts were focused on RT strength.<sup>[11,12]</sup> The key to establishing the comprehensive high performance of alloy + CNT composites is the “good dispersion” of CNTs, which entails several aspects. It is well appreciated that brittleness can be reduced by disaggregating inclusions and keeping the characteristic length scale of an individual inclusion at below tens of nanometers.<sup>[3]</sup> One certainly does not want voids between CNTs and metal matrix, and hopes the dispersion of CNTs does not significantly delay the sample from achieving 99% of the theoretical density. Lastly, it has been shown empirically that nanoprecipitation/particles in metals and alloys should be better situated in the grain interior (intragranular) than on the GB, in order to increase mechanical strength while preserving/extending the ductility.<sup>[13,14]</sup> This is probably because GBs are 2D and also naturally form a percolating network, while CNTs are 1D and precipitate/particles are 0D. Fracture favors percolating 2D flaws (cracks are 2D) by virtue of elasticity, whereas interfacial debonding along 1D and 0D flaws, even if it happens, are less dangerous from a stress intensity factor point of view. GBs themselves are already excellent flow strengthening agents by forcing dislocation slip to change direction.<sup>[15]</sup> Adding CNTs right on GBs will likely further strengthen the flow strength, but may also cause the GB cohesion strength to go down, and once some debonding has happened fracture may propagate much quickly along a 2D percolating GB network. So, intragranular dispersion of CNTs should be recommended relative to intergranular dispersion of CNTs.

However, for the metal + CNT nanocomposite, besides conventional problems mentioned above, the oxide layer on metal, the difference in surface tension between metal and CNTs and wetting of CNTs, and bonding strength of metal + CNT interface are other critical factors to be overcome. For example, the oxide layer formed on the surface of metal is detrimental to uniform dispersion of CNTs in metal matrix since mechanically robust nanosize oxide layer acts as a strong barrier to the CNT trying to penetrate inside the grain.<sup>[16–18]</sup> Such an oxide layer segregates CNTs from being uniformly distributed inside the metal matrix, consequently limiting its dispersion. Even if the oxide layer can be broken, the high surface tension of metals and poor adhesion of carbon would resist mixing CNTs in metal.

Intragranular dispersion in metals and alloys were often induced through thermal precipitation<sup>[14,19]</sup> and liquid phase processing.<sup>[20]</sup> However, these methods are limited due to the thermochemical stability requirement on the particles. In comparison to these methods, mechanical alloying (MA) provides

more freedom to choose the matrix and particles.<sup>[21]</sup> Deformation and cold welding of metals at nanoscale are much different from those of the bulk. Surface allows fast atomic diffusion.<sup>[22]</sup> Especially, when the metal particle size reaches near 10 nm, crystalline metals show viscous deformation and thus the envelopment easily occurs without applying much external force, showing liquid-like behavior even though the interior remains crystalline.<sup>[23]</sup> This liquid nature of metallic surface provides an opportunity to mix thermodynamically unstable/incompatible phases such as CNT.

In situ TEM observations verify the liquid-like envelopment mechanism of the intragranular dispersion of CNT in Al via cold welding derived from rapid surface diffusion of Al. The oxide-free Al was prepared under in situ TEM by applying tension to sample until fracture occurred (Figure S8, Supporting Information). We then transferred a CNT on the bare Al surface by manipulating the sample with a piezo-actuator equipped in Nanofactory scanning tunneling microscopy (STM)-TEM holder. The two bare surfaces of Al started to weld via surface diffusion after contacting each other, to minimize the surface energy.<sup>[23]</sup> The CNT was covered by Al (Figure 4A). Since the cold welding forced the two Al pieces to squeeze the CNT into the middle and became one piece, necking and fracture took place as they have pulled apart (Figure 4B). The fracture point was different from the welded interface, leaving a fraction of Al still attached to the lower part of the upper Al, covering the CNT (Figure 4C and Movie S3, Supporting Information). By repeating this process, the CNT was totally embedded into the Al matrix. This shows good wetting of Al onto CNT when there is no oxide layer.

We quantitatively analyze the surface diffusivity from in situ TEM by taking the flattening time of a curved surface after the coverage of CNT via cold welding (Figure S12, Supporting Information).<sup>[24–26]</sup> The surface diffusivity  $D_s$  can be estimated by the following equation<sup>[26]</sup>

$$D_s = -\frac{Sk_B T}{v\gamma_M \Omega^2} \left( \frac{\lambda}{2\pi} \right)^4 \quad (1)$$

where  $S$  is the slope from the natural logarithm of height versus a linear function of time in Figure S13A in the Supporting Information,  $\Omega$  is atomic volume (0.0166 nm<sup>3</sup> per atom),  $T$  is room temperature (298 K),  $v$  is the surface atomic density ( $v_{(111)} = 0.1 \text{ atom nm}^{-2}$ ), and  $\lambda$  is the segment length in the rest position (24 nm in this case). The surface diffusivity ( $D_s$ ) is estimated to be  $3.27 \times 10^{-11} \text{ cm}^2 \text{ s}^{-1}$  at room temperature. The value is very close to the empirical diffusivity of the surface,  $1.8 \times 10^{-11} \text{ cm}^2 \text{ s}^{-1}$  at room temperature.<sup>[24]</sup> The activation energy of the atomic self-diffusion was previously reported in Table S2 in the Supporting Information.<sup>[24]</sup> The surface diffusivity  $D_s$  is higher than those of GB, dislocation, and bulk.<sup>[24]</sup> Since the surface state is dynamic instead of the rigid in nanoscale, atoms easily diffuse through surface, like a viscous “2D liquid.”<sup>[23]</sup> The fluid nature observed in in situ TEM agrees reasonably with our MA ball milling experiment. Ball milling is a dynamic condition. Impact and shearing between ball-ball or ball-container continuously deform and refine the Al nanoparticles, exposing bare surfaces. The volume fraction of surface atoms increases as the particle size decreases. At below

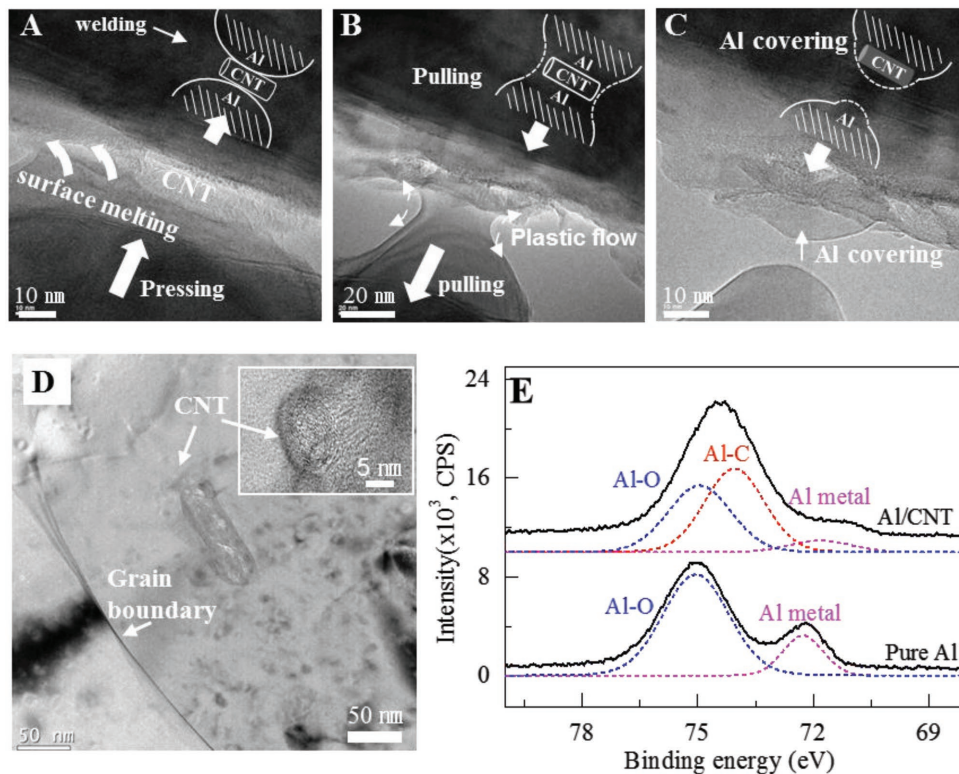


**Figure 4.** In situ TEM observation of the mechanism of CNT embedding in Al under no-oxidation conditions. A–C) CNT embedment via surface melting process: A) surface melting-driven cold welding on the contact area, B) Al disconnected through plastic flow, and C) residual Al covered on the top of CNT. See Movie S3 in the Supporting Information. D) TEM observation for the nanoscopic dispersion shows CNTs in the Al grain interior (inset: The intact wall structure of intragranular CNT, 3.3 Å interlayer distance of the graphitic layer). E) Al 2p peak in XPS of pure Al (bottom) and Al + CNT 10 wt% at 600 °C during SPS (top).

100 nm, 1 vol% of the atom occupies the surface which is comparable to the volume fraction of the CNTs (Figure S13C, Supporting Information).

To induce this diffusion-driven cold welding in MA, free random movement of atoms on the surface is an essential condition. Thus, the formation of the oxide layer in Al particles needs to be prevented. Chen et al. reported that purging of argon into the ball mill container would not inhibit oxidation of Al during ball milling.<sup>[27]</sup> To satisfy the required condition to enhance the atomic diffusion above, we designed ball milling inside the Ar-filled glove box (<0.1 ppm O<sub>2</sub>, <0.1 ppm moisture). Al was reported to be oxidized by exposing to 10<sup>-6</sup> torr vacuum for 100 s.<sup>[28]</sup> 0.1 ppm of oxygen is two orders higher concentration of oxygen than 10<sup>-6</sup> torr, hence the glove box environment is equal to 1 s exposure in the same vacuum condition. As the ball milling is a dynamic condition where the frequency of collision event of the ball is >10<sup>4</sup> s<sup>-1</sup>,<sup>[29]</sup> 1 s is more than enough to allow for anchoring CNT on bare Al surface to induce surface diffusion and cold welding before reoxidation ( $\approx$ 10<sup>11</sup> CNTs are embedded each second). Furthermore, the temperature inside of the ball mill container is  $\approx$ 200 °C, which makes the diffusivity three order higher than that at RT.<sup>[30]</sup> This condition makes CNTs completely feel the liquid-like aluminum on the surface, with plenty of opportunities to get enveloped. For better cold welding, we disaggregated the CNT clusters and located them on the surface of Al particles using a high-speed

blade mixer (decluster). The declustered individual CNTs on Al surface were further ball milled to induce cold welding and encapsulation of CNTs into Al. After declustering of CNTs, the number of CNTs on the Al is  $\approx$ 90  $\mu\text{m}^{-2}$  which is small enough to enable the embedding of all the CNTs into the Al matrix during the ball milling. This step creates a high concentration of CNTs in the master alloy which is essential for the tons-scale industrial application. The encapsulated CNTs in the master alloy have an intimated interface through Al–C bonding<sup>[31]</sup> and Si–C bonding. It consequently allows dispersion into macroscopically molten Al alloys (see Supporting Information Movie S2) without significant segregation of CNTs.<sup>[1,2]</sup>

To verify the nanodispersion of CNTs (individual CNTs) in bulk Al + CNT composites, confocal Raman and TEM were used. The CNTs were mostly located inside the grains, as shown in the TEM image (Figure 4D). This result contrasts starkly with ball milling without controlling the environmental oxidation, where CNTs are strongly localized at the Al particle boundaries due to the limited atomic diffusion near the Al surface oxide layer (Figures S9 and S10, Supporting Information). Consequently, less improvement in the tensile strength and more degradation in fracture strain were observed (Figure S11, Supporting Information). This shows the comprehensive enhancement of properties is intimately related to the surface condition of Al during ball milling in creating the master alloy.

The linear increase in Young's modulus at CNT concentrations up to 1 wt% (Figure S16, Supporting Information) clearly indicates efficient load transfer through the formation of a strong interfacial bonding between Al and CNT surfaces. The Al–C covalent bonds were confirmed from X-ray photoelectron spectroscopy (XPS) spectra (Figure 4E). A large portion of the Al–C peak was generated in the Al + CNT composite, whereas aluminum oxide peak was not as prominent as that of pure Al. The related  $\text{Al}_4\text{C}_3$  peaks in the X-ray diffraction (XRD) patterns and the blueshifting of G-band in Raman are also clear evidence of strong interfacial bonding (see the characterization of the interfacial bonding in the Supporting Information).

## 5. Conclusion

The quantitative contribution of CNTs to mechanical strength enhancement can be analyzed using the strengthening efficiency ( $R$ ),  $R \equiv (\sigma_c - \sigma_m)/v_c \sigma_m$ , where  $\sigma_c$  and  $\sigma_m$  are the tensile strengths of the composite and matrix, respectively, and  $v_c$  is the volume fraction of CNTs to metal, is the change in strength by adding unit volume of CNTs.<sup>[32]</sup> The strengthening efficiency is generally influenced by the degree of CNT dispersion and interfacial strength. Figure 5 summarizes the relationship of these properties with different materials manufacturing methods. Since an intragranular nanodispersion strategy of CNTs in Al matrix leads to enhanced mechanical strength with a tenable ductility, both strengthening efficiency and toughness are consistently enhanced with an addition of CNTs. All our data for the different alloys show the best values for specific toughness versus specific strengthening efficiency among reported literature. The significantly improved high-temperature creep capability (by 70 °C or 0.08 $T_M$ ), the excellent electrical and thermal conductivities, the acceptable cost, and the wide applicability of this method to both pure Al and Al alloys (2000, 6000, and 7000 series) mean the intragranular dispersion of 1D nanowires and nanotubes is a new paradigm for making high-performance structural materials.

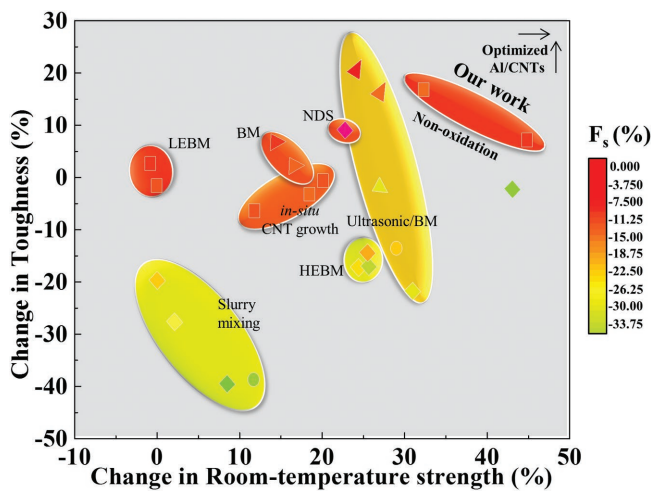


Figure 5. A plot of change in room-temperature tensile strength, toughness, and fracture strain ( $F_s$ ) by adding 1 vol% of CNTs.

## 6. Experimental Section

*Intragranular Dispersion of CNT in Al:* The master alloy was made by RT ball milling in Ar environment. Subsequently, it can be further downblended by impeller-driven mixing in the molten state in the same alloy matrix (see Movie S2, Supporting Information). After the surface modification, the tangled MWCNTs were unraveled by a high-speed blade mixer (VM0104, Vita-Mix, USA) for 20 min at max. 37 000 rpm, which split the clusters into single strands of CNT on the surface of Al particles. The declustered CNTs were then buried inside the Al particles using a planetary ball mill for 30 min at 250 rpm in a glove box under less than 0.1 ppm of oxygen and moisture to prevent oxidation. As a consequence of the cold welding, CNTs are encapsulated inside Al grains, creating the master alloy (Figure 2A). The master alloy can then be further processed by SPS, billetization, or melting process/casting to create bulk specimen. SPS consolidated the granules and formed the interfacial Al–C covalent bonds. The sintering conditions were optimized to yield a density greater than 99% of the theoretical value by controlling the temperature and time. The high relative density was obtained due to the encapsulation of CNTs inside the Al particles, i.e., no void volume was produced by CNT agglomeration on the particle boundaries. Microstructural observations demonstrate that the oxide layer on the Al granule surfaces was successfully disintegrated by the SPS process, forming discrete oxide nanoparticles. For the melt process, thin SiC layer was decorated on the surface of the CNT to improve the wetting to molten Al.<sup>[2]</sup> 5 wt% SiC/CNTs of the master alloy subsequently dissolved into molten Al alloy to become 0.5 wt% CNT while stirring with a graphite impeller in a vacuum ( $10^{-3}$  torr). The consolidated Al + CNT was further shaped by milling, extrusion, and rolling (detailed experimental parameters are described in Table S1, Supporting Information).

*Fabrication of CNTs + Al Alloy Composite:* Cu (1 wt%) was added for the 2000 series and Zn (5.6 wt%), Mg (2.5 wt%), and Cu (1.6 wt%) were added for 7000 series to pure Al. For the 6000 series alloy-CNT composite, the Al 6063 ingot was atomized to powder and proceeded with the same procedure. After shaping (extrusion, rolling, and milling), all the alloys were subjected to T6 tempering including solution heat treatment and aging treatment, before the mechanical properties were measured (Table S1, Supporting Information).

*Characterization of Mechanical/Thermal/Electrical Properties:* Mechanical properties were characterized using an ultimate tensile tester (Landmark 25 kN, MTS, USA) and a micro-Vickers hardness tester (HM-211, Mitutoyo, Japan). The tensile specimen was prepared using a mechanical mill with a 6 mm gage diameter and a gage length of 25 mm (E8/E 8M-08, ASTM). The tensile test was performed at a speed of 2 mm min<sup>-1</sup>. The hardness test was conducted on a cross-section of the specimen using a load of 100 g for 10 s. The thermal conductivity was determined by laser flash analysis. The electrical conductivity was determined by measuring the electrical resistance of a metallic wire as well as four-probe method to measure the sheet resistance. The high-temperature creep properties were characterized by applying a dead load and measuring the strain rate in the DMA (Q800, TA instrument), and creep fracture temperature ( $T_f$ ) measurement using conventional dog bone shape specimen with pin-hole on the grip part after 400 °C for 32 h annealing treatment. For the DMA measurement, the Al + CNT composite was thinned down to 100 μm by cold rolling and applying 70 MPa engineering stress at 300 °C. For the  $T_f$  measurement, a pin-loaded tensile specimen was made modified from ASTM E8 with 50 mm total length, 20 mm gauge length, and 2 mm of thickness. The temperature was linearly increased until fracture occurred. The applied load in the  $T_f$  experiment was half of RT yield strength of the respective material, where the RT yield strength was converted from RT Vickers hardness.

*In Situ TEM Observations:* An in situ TEM experiment was conducted to verify the nanoscale mechanism of atomically surface-diffusion driven cold welding of Al for dispersing and locating the CNT inside Al grain. Nanofactory STM-TEM holder equipped with 3D piezo-manipulator was used for this experiment (Figure S8A, Supporting Information, left picture). T-shaped Al sample with thickness ≈100 nm was prepared using focused ion beam (FIB) and transferred to the tip of a W probe

and welded by Pt electron beam deposition inside a scanning electron microscopy (Helios Nanolab 600 Dual Beam FIB Milling System) as shown in Figure S8B in the Supporting Information. W probe with a hook-shaped tip was prepared using the same system to pull the Al sample in situ inside TEM (JEOL 2010F). The oxide-free Al was prepared inside in situ TEM by applying tension to the FIB-cut sample until fracture (Figure S8A, right, Supporting Information). A CNT was then transferred on the bare Al surface by manipulating the sample with a piezo-manipulator as shown in Figure S8C,D in the Supporting Information.

## Supporting Information

Supporting Information is available from the Wiley Online Library or from the author.

## Acknowledgements

The authors acknowledge support by NSF DMR-1410636. This research was also supported by Institute for Basic Science (IBS-R011-D1) and Basic Science Research Program through the National Research Foundation of Korea (NRF) funded by the Ministry of Education, Science and Technology (NRF-2013R1A6A3A03064138) and Ministry of Science and ICT (NRF-2017R1A2A1A17069427). K.P.S. designed and developed the work. A.K. performed the in situ TEM measurement. J.G.P. and D.H.K., and H.Y.J. optimized the fabrication condition of Al/CNT composite. X.L. performed the theoretical analysis. S.H.J. and H.S.K. analyzed dislocation density and microstrain. H.K. contributed to discovering the intragranular dispersion of CNTs in TEM. J.L. and Y.H.L. guided and analyzed the work. K.P.S., J.L., and Y.H.L. wrote the paper. All authors participated in the paper review.

## Conflict of Interest

The authors declare no conflict of interest.

## Keywords

aluminum, carbon nanotubes, creep, in situ transmission electron microscopy, intragranular

Received: January 22, 2018  
Published online:

- [1] K. P. So, X. Liu, H. Mori, A. Kushima, J. G. Park, H. S. Kim, S. Ogata, Y. H. Lee, J. Li, *Extreme Mech. Lett.* **2016**, 8, 245.
- [2] K. P. So, J. C. Jeong, J. G. Park, H. K. Park, Y. H. Choi, D. H. Noh, D. H. Keum, H. Y. Jeong, C. Biswas, C. H. Hong, *Compos. Sci. Technol.* **2013**, 74, 6.

- [3] H. Gao, B. Ji, I. L. Jäger, E. Arzt, P. Fratzl, *Proc. Natl. Acad. Sci. USA* **2003**, 100, 5597.
- [4] W. M. Daoush, B. K. Lim, C. B. Mo, D. H. Nam, S. H. Hong, *Mater. Sci. Eng. A* **2009**, 513, 247.
- [5] C. Xu, B. Wei, R. Ma, J. Liang, X. Ma, D. Wu, *Carbon* **1999**, 37, 855.
- [6] J. Svensson, E. E. B. Campbell, *J. Appl. Phys.* **2011**, 110, 111101.
- [7] Y. H. Lee, K. P. So, H. K. Park, E. S. Kim, *Korea Patent* 10-1114628, **2012**.
- [8] S. Cho, K. Kikuchi, T. Miyazaki, K. Takagi, A. Kawasaki, T. Tsukada, *Scr. Mater.* **2010**, 63, 375.
- [9] J. Wu, H. Zhang, Y. Zhang, X. Wang, *Mater. Des.* **2012**, 41, 344.
- [10] G. Gonzalez-Doncel, O. Sherby, *Acta Metall. Mater.* **1993**, 41, 2797.
- [11] S. R. Bakshi, D. Lahiri, A. Agarwal, *Int. Mater. Rev.* **2010**, 55, 41.
- [12] S. R. Bakshi, A. Agarwal, *Carbon* **2011**, 49, 533.
- [13] G. Liu, G. J. Zhang, F. Jiang, X. D. Ding, Y. J. Sun, J. Sun, E. Ma, *Nat. Mater.* **2013**, 12, 344.
- [14] P. V. Liddicoat, X. Z. Liao, Y. H. Zhao, Y. T. Zhu, M. Y. Murashkin, E. J. Lavernia, R. Z. Valiev, S. P. Ringer, *Nat. Commun.* **2010**, 1, 63.
- [15] T. Zhu, J. Li, A. Samanta, H. G. Kim, S. Suresh, *Proc. Natl. Acad. Sci. USA* **2007**, 104, 3031.
- [16] H. Kwon, M. Estili, K. Takagi, T. Miyazaki, A. Kawasaki, *Carbon* **2009**, 47, 570.
- [17] T. Zhu, J. Li, *Prog. Mater. Sci.* **2010**, 55, 710.
- [18] J. Y. Huang, L. Zhong, C. M. Wang, J. P. Sullivan, W. Xu, L. Q. Zhang, S. X. Mao, N. S. Hudak, X. H. Liu, A. Subramanian, H. Y. Fan, L. A. Qi, A. Kushima, J. Li, *Science* **2010**, 330, 1515.
- [19] Y. H. Zhao, X. Z. Liao, S. Cheng, E. Ma, Y. T. Zhu, *Adv. Mater.* **2006**, 18, 2280.
- [20] K. Lu, L. Lu, S. Suresh, *Science* **2009**, 324, 349.
- [21] C. Suryanarayana, *Prog. Mater. Sci.* **2001**, 46, 1.
- [22] R. Tromp, *Nat. Mater.* **2003**, 2, 212.
- [23] J. Sun, L. He, Y.-C. Lo, T. Xu, H. Bi, L. Sun, Z. Zhang, S. X. Mao, J. Li, *Nat. Mater.* **2014**, 13, 1007.
- [24] C. M. Tan, A. Roy, *Mater. Sci. Eng., R* **2007**, 58, 1.
- [25] M. E. Keeffe, C. Umbach, J. M. Blakely, *J. Phys. Chem. Solids* **1994**, 55, 965.
- [26] D.-G. Xie, Z.-J. Wang, J. Sun, J. Li, E. Ma, Z.-W. Shan, *Nat. Mater.* **2015**, 14, 899.
- [27] B. Chen, J. Shen, X. Ye, L. Jia, S. Li, J. Umeda, M. Takahashi, K. Kondoh, *Acta Mater.* **2017**, 140, 317.
- [28] A. Arranz, C. Palacio, *Surf. Sci.* **1996**, 355, 203.
- [29] H. Mio, J. Kano, F. Saito, K. Kaneko, *Mater. Sci. Eng. A* **2002**, 332, 75.
- [30] M. Li, D.-G. Xie, E. Ma, J. Li, X.-X. Zhang, Z.-W. Shan, *Nat. Commun.* **2017**, 8, 14564.
- [31] K. P. So, E. S. Kim, C. Biswas, H. Y. Jeong, D. H. Keum, K. H. An, Y. H. Lee, *Scr. Mater.* **2012**, 66, 21.
- [32] L. Jiang, Z. Q. Li, G. L. Fan, L. L. Cao, D. Zhang, *Scr. Mater.* **2012**, 66, 331.



## Supporting Information

for *Adv. Sci.*, DOI: 10.1002/advs.201800115

### Intragranular Dispersion of Carbon Nanotubes Comprehensively Improves Aluminum Alloys

*Kang Pyo So, Akihiro Kushima, Jong Gil Park, Xiaohui Liu,  
Dong Hoon Keum, Hye Yun Jeong, Fei Yao, Soo Hyun Joo,  
Hyoung Seop Kim, Hwanuk Kim, Ju Li,\* and Young Hee Lee\**

## SUPPLEMENTARY INFORMATION

### Materials and Methods

#### A. Fabrications

##### Sample preparation

The uniform dispersion of CNTs into Al grains was achieved from the three main factors, (i) the CNT declustering, (ii) cold-welding and (iii) interfacial bonding. The flow chart of processes is shown in Fig. 1. Depending on the post-process such as melt blending and sintering, type of the surface modification is required to enhance the wetting and the interfacial strength. The surface of CNT can be modified by the organic functional group, defects or inorganic layer such as SiC and  $\text{Al}_2\text{O}_3$ .

The SiC layer decorated by thermal decomposition in previous report.<sup>1</sup> The diameter and length of the multi-walled (MW) CNTs (CM95, Hanwha Nanotech, Korea) were in the range of 10–30 nm and a few tens of micrometers, respectively. A 1:1 atomic ratio mixture (7:3 by weight ratio) of Si powder (325 mesh, 99%, Aldrich) to MWCNTs were mechanically crushed using a planetary ball miller (Pulverisette 6, Fritsch, Germany) for 10 h at 230 rpm with 5 mm zirconia balls. Additional MWCNTs were added to this crushed mixture. Different mixing ratios (3:5, 6:5, 12:5 and 20:5) of the crushed mixture to MWCNTs were investigated. To form SiC on the MWCNT surfaces (SiC/CNT), high-temperature annealing was performed at 1300 °C for an hour in a vacuum induction furnace.

The  $\text{Al}_2\text{O}_3$  particles are decorated by the microwave treatment after anchoring aluminum precursor. 1~5g of aluminum tri-acetyl acetonate were decorated in 1 g of MWCNT in 0.5g poly acrylic acid in water. After coating of the aluminum precursor on the MWCNT, the samples are completely dried and place into microwave oven under argon atmosphere. Thermal spikes were observed during the microwave irradiation for 5 min. After the microwave treatment, uniform coating of  $\text{Al}_2\text{O}_3$  were seen on the surface of CNT as shown in Fig. S1

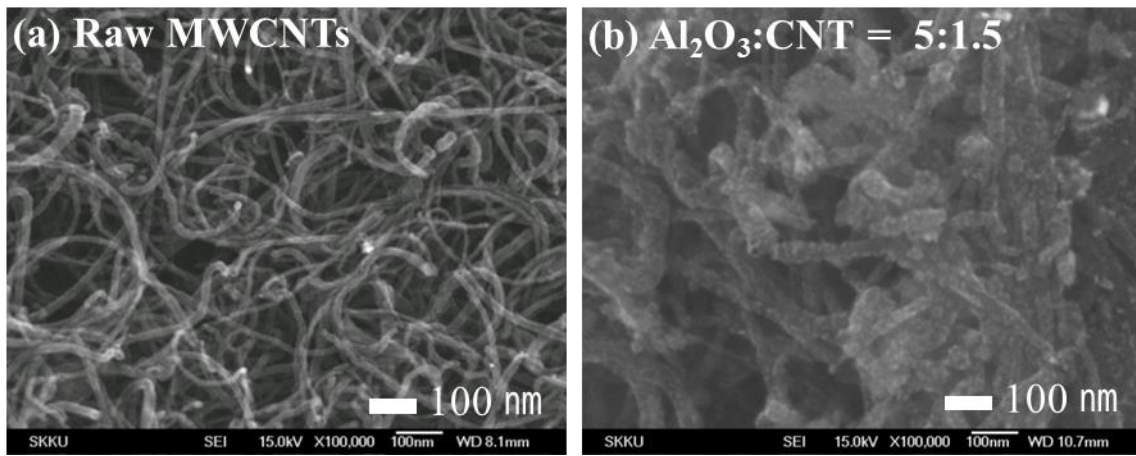


**Fig. S1 SEM images after Al<sub>2</sub>O<sub>3</sub> decoration on CNTs.** (a) Raw MWCNTs and (b) decoration of Al<sub>2</sub>O<sub>3</sub> particles on CNTs after microwave treatment.

The declustering process of CNT on the surface of Al particles was performed by a high-speed blade mixer (VM0104, Vita-Mix, USA) to unravel the tangled multiwalled carbon nanotubes (MWCNTs), (CM95, Hanwha Nanotech, Korea) for 20 min at max. 37,000 rpm (Fig. S2B and Fig. S3C). The declustered CNTs were cold-welded using a planetary ball miller (J.E. Powder, Korea) for 30 min at 250 rpm to produce the master alloy, as shown by the Al/CNT granule in Fig. S2D and Fig. S2D. The process was completed in a glove box (M.O. Tech, Korea) under less than 1 ppm of oxygen and moisture to prevent oxidation. For the CNT volume calculation, a CNT density of 1.3 g/cm<sup>3</sup> was used. The concentration of CNTs was varied from 0.1 wt% to 5 wt%. As a consequence of the cold-welding, CNTs are encapsulated in Al particles that were further consolidated under 40 MPa with spark plasma sintering (SPS, 50 t, 50 kW, Eltek, Korea) to form interfacial Al-C covalent bonds at 560 °C for 15 min (Fig. S2E). The bulk Al/CNT composites were extruded from 2.5 mm to 8 mm in diameter with an extrusion ratio of 9:1 at 550 °C (Fig. S2E and Fig. S3E).

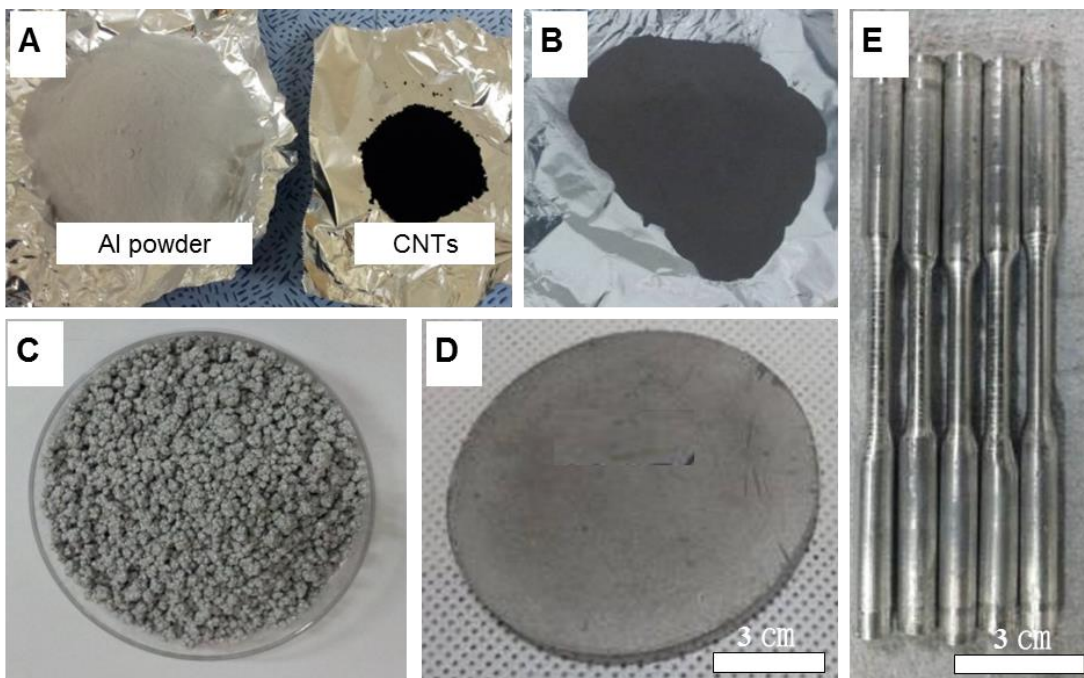


**Fig. S2 Schematic illustration for fabricating Al+CNT composite via surface melting-driven cold welding and sample photos for each process.** (A) The Al powder and the pristine CNT powder, (B) after the declustering process of 2 vol% CNT, (C) after encapsulation of 0.4 vol% CNT, (D) after SPS of Al/CNT 0.4 vol%, and (E) after extrusion of Al/CNT 0.4 vol%. The change of powder color from grey to black indicates that individual CNT was attached on the surface of Al particles after declustering process as (B). CNTs were encapsulated during mechanical ball mill in a glove box, forming 2 mm diameter granules, as shown in (C). The color was converted into grey, ensuring encapsulation of CNTs inside Al particles. The complete CNTs encapsulation was further verified by bright silver color after extrusion (E).

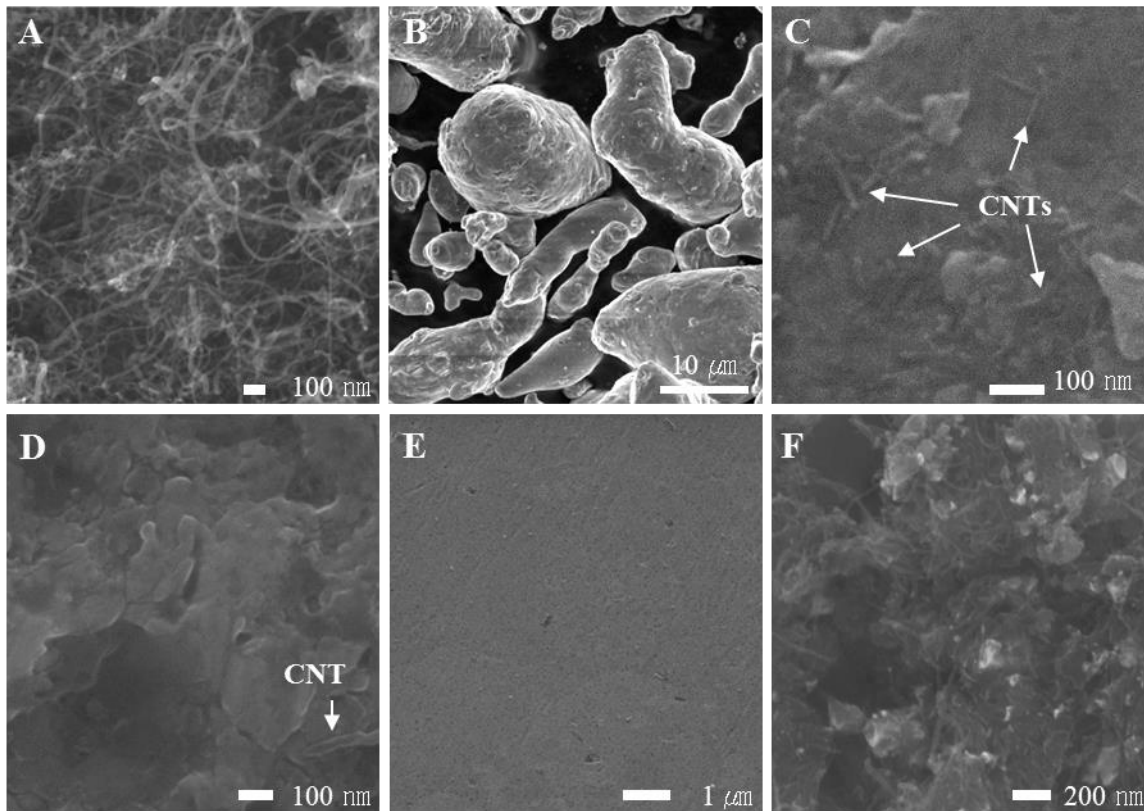


**Fig. S3 SEM images for each step.** (A) Raw CNTs, (B) raw Al powder, (C) Al/CNT composite after 2 vol% CNT declustering process. Individual CNTs were visible on the surface of Al particles. (D) Master alloy after encapsulation of 0.4 vol% CNTs. (E) Al/CNT composite after SPS and extrusion, and (F) CNTs embedded inside Al, which appeared after acid etching. The diameter and length of MWCNTs were in the range of 10~30 nm and a few tens micrometers, respectively (A). The purchased gas-atomized aluminum powder was filtered by 200 meshes to have particle sizes less than 50 microns, as shown in (B). Individual CNTs were observed on the surface of Al particles after declustering process, as shown in (C). The declustered CNTs were embedded inside Al particles after oxygen-free mechanical pulverization-assisted encapsulation process, as shown in (D). Al particles were fractured. The bare surface was exposed without oxidation during mechanical pulverization. The fractured Al particles were coalesced to each other during further pulverization process, forming CNT-embedded Al granules. The CNT morphology (1 μm length) was well maintained and detected after the final process, as shown (F).

To see the influence of CNT in the precipitation strengthened alloys, we prepared Al alloys/CNT composites. The alloy elements were introduced during ball milling (mechanical alloying). We add Cu (1 wt%) for the 2000 series and Zn (5.6wt%), Mg (2.5 wt%), Cu (1.6wt%) for 7000 series to pure Al. For the 6000 series alloy-CNT composite, we atomized the Al 6063 ingot to powder and proceeded with the same procedure. All the alloys were subjected to T6

tempering including solution heat treated and aging treated. The detailed experiment parameters are described in Table S1.

**Table S1. Fabrication process and characterization of Al alloy CNT**

Matrix	Interface	Dispersion process	Bulk formation	Shape forming	Heat treatment	Properties
	Al-C	mixer/ball mill	SPS	Extrusion	N/A	Tension, hardness, electric/thermal conductivity
Pure Al				Extrusion/rolling	Annealing 350°C/5h	Creep/ $T_f$
	Si-C <sup>1</sup>	mixer/ball mill	Melt blending	extrusion	N/A	Tension
	Al <sub>2</sub> O <sub>3</sub>	mixer/ball mill	Melt belding	extrusion	N/A	Tension
2000 serise	Al-C	Multi-step Ball mill	Compacting	extrusion	Induction heating 550 °C/1h, natural aging	Tension
6000 serise	Al-C	mixer/ball mill	SPS	extrusion	530°C/4h, 175°C/8h	Tension
7000 serise	Al-C	mixer/ball mill	SPS	extrusion	480°C/24h, liquid N <sub>2</sub> quenching, 100 °C/5h	Tension
AlCu/AlSiMg	Al-C	mixer/ball mill	SPS	extrusion	530°C/4h, 175°C/8h	Tension
AlDC 12.2	Si-C <sup>2</sup>	Ball mill	Melt blending	casting	N/A	Electric resistivity

## SPS optimization

We optimized the sintering conditions to yield an Al+CNT composite with a density greater than 99% of the theoretical value by controlling the temperature and time, as shown in Fig. S4A and B, respectively. To achieve a relative density of 99%, a sintering temperature of 560 °C was used with a sintering time of 15 min at a pressure of 46 MPa. The increased relative density was easily obtained because CNTs were encapsulated inside the Al particles, i.e., no void volume was produced by CNT residence in the particle boundaries. Microstructural observations demonstrate that the oxide layer on the Al granule surfaces was successfully disintegrated by the SPS process, forming discrete oxide nanoparticles, as shown in Fig. S5A to C.<sup>3,4</sup>

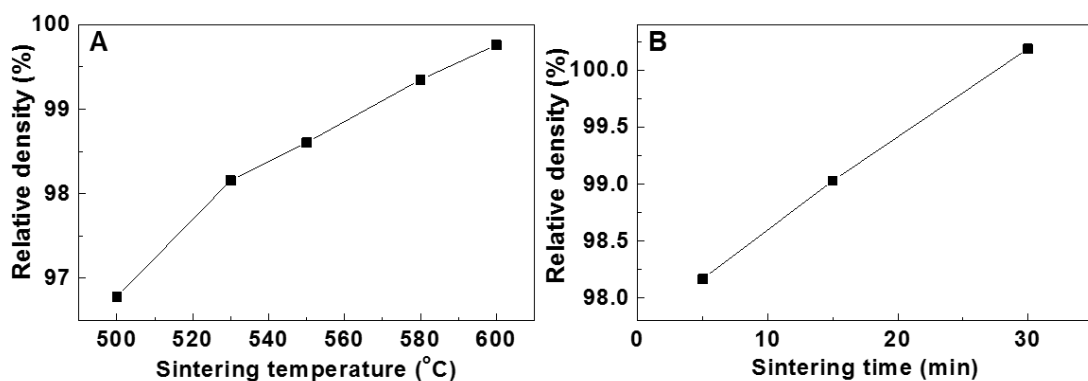


**Fig. S4 Sintering process-dependent relative density compared to that of the Al/CNT composite.** (A) The sintering temperature- and (B) sintering time-dependent relative densities. The reference density was calculated by,  $\rho_{\text{Ref.}} = \frac{\rho_{\text{CNT}}\rho_{\text{Al}}}{\rho_{\text{CNT}}m_{\text{Al}} + \rho_{\text{Al}}m_{\text{CNT}}}$  where  $\rho_{\text{CNT}}$ ,  $\rho_{\text{Al}}$ ,  $m_{\text{CNT}}$  and  $m_{\text{Al}}$  are CNT density, Al density, CNT weight fraction and Al weight fraction, respectively. A CNT density of 1.3 g/cm<sup>3</sup> was used. The relative density was obtained from experimental density divided by the reference density. The increased relative density to nearly to 100% was easily obtained because CNTs were encapsulated inside the Al particles, i.e., no dead volume was produced by CNT residence in the particle boundaries. To achieve high-density more than 99 % relative density, 580 °C and 15 min of the sintering temperature and time were used.

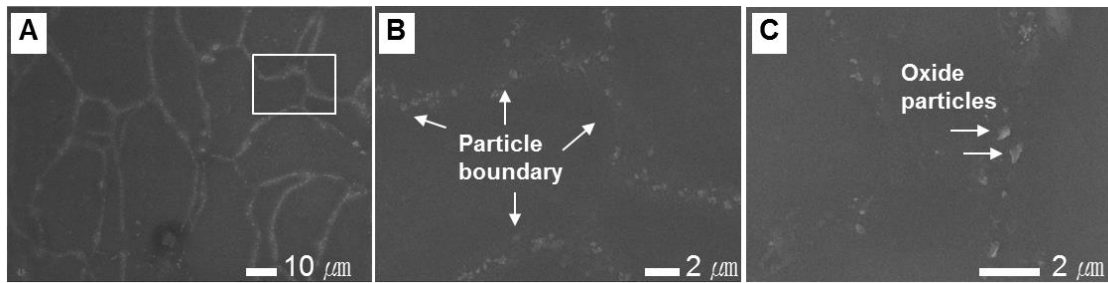


**Fig. S5 Microstructure observations after SPS at 580 °C for 15 min with 2 vol% CNT.** (A) A particle boundary trace indicated by white lines, (B) enlarged in (A), and (C) oxide nanoparticles. The oxide layer on the surface of Al granules was formed after encapsulation during sample transfer for SPS. Note that CNTs were already well dispersed inside Al granules. Microstructural observations demonstrate that the oxide layer on the encapsulated Al granule surfaces was successfully disintegrated by the SPS process, forming discrete oxide nanoparticles.

### B. High-temperature capability test.

The Al+CNT samples are rolled down to 2mm by cold rolling. We made the pin-loaded tensile specimen modified from ASTM E8 with 50mm of total length and 20mm of gauge length. The applied force was determined by half of yield strength where the yield strength was converted from Vickers hardness. The parameters are described in Table S2. We use ASTM E4 standard calibrated equipment (ATS applied test system INC.). All the sample were heat treated under 400°C for 32hrs to release the internal micro strain during the sample preparation. The heating rates were 100°C/hr up to fracture. The elongation vs temperature is shown in Fig. S6. The fractured temperatures ( $T_f$ ) are determined after the final fracture.

**Table S2. Applied force for high-temperature capability**

Samples	Hardness (Hv)				Av.	Yield st. (MPa)	0.5 $\sigma_y$
Control Al	58	56	57	56	56(±0.5)	109	54
0.5 wt%	70	66	67	73	69(±1.6)	124	62
1 wt%	78/75	89/85	66/72	79/74	77(±2.6)	134	67

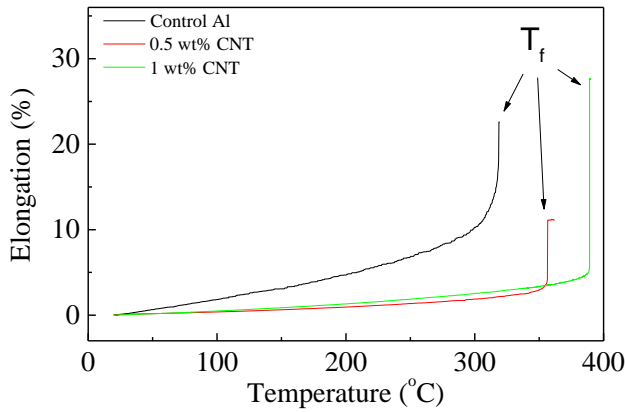


**Fig. S6** Elongation of Al+CNT at a different temperature.

The strain rates were measured in the Dynamic mechanical analyzer (DMA, Q800, TA instrument). The sample was thin down to 100um by rolling. Thin films were used to measure the strain rate. All the films were heat treated 350°C for 5hrs.

### C. Electrical and thermal conductivity.

We have used the four probe method to measure electrical conductivity after extrusion 2 mm of diameter. To measure accurate electrical conductivity, we extrude the length to 1 m. For the comparison purpose, we fabricate Al alloy +CNT composite by using melt-processing with the ALDC 12.2 die-casting alloy as a matrix. We measure the 4 probes electrical resistance on the surface by using Van der Pauw method after polishing the surface enhance the contact. The measured area is 1 cm<sup>2</sup> on the surface of Al+CNT composite after casting. The resistance is shown in Fig. S7. The thermal conductivity was characterized by Laser flash analysis (LFA) after shaping 1cm x 1cm with 1mm thickness samples.

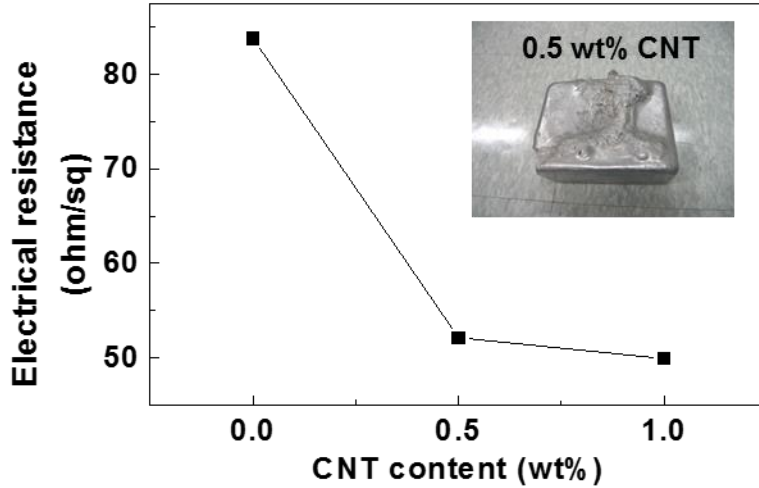


**Fig. S7 Surface resistant of the Al+CNT composite.**

#### D. *In-situ* TEM observations

We conducted an *in-situ* TEM experiment to verify the nanoscale mechanism of atomically surface-diffusion driven cold-welding of Al for dispersing and locating the CNT inside Al grain. Nanofactory STM-TEM holder equipped with 3D piezomanipulator was used for this experiment (Fig. S8A, left picture). T-shaped Al sample with thickness ~100 nm was prepared using focused ion beam (FIB) and transferred to the tip of a W probe and welded by Pt electron beam deposition inside a scanning electron microscopy (Helios Nanolab 600 Dual Beam FIB Milling System) as shown in Fig. S8B. W probe with a hook-shaped tip was prepared using the same system to pull the Al sample *in-situ* inside TEM (JEOL 2010F). The oxide-free Al was prepared inside *in-situ* TEM by applying tension to the FIB-cut sample until fracture (Fig. S8A, right). We then transferred a CNT on the bare Al surface by manipulating the sample with a piezo-manipulator as shown in Fig. S8C and D.

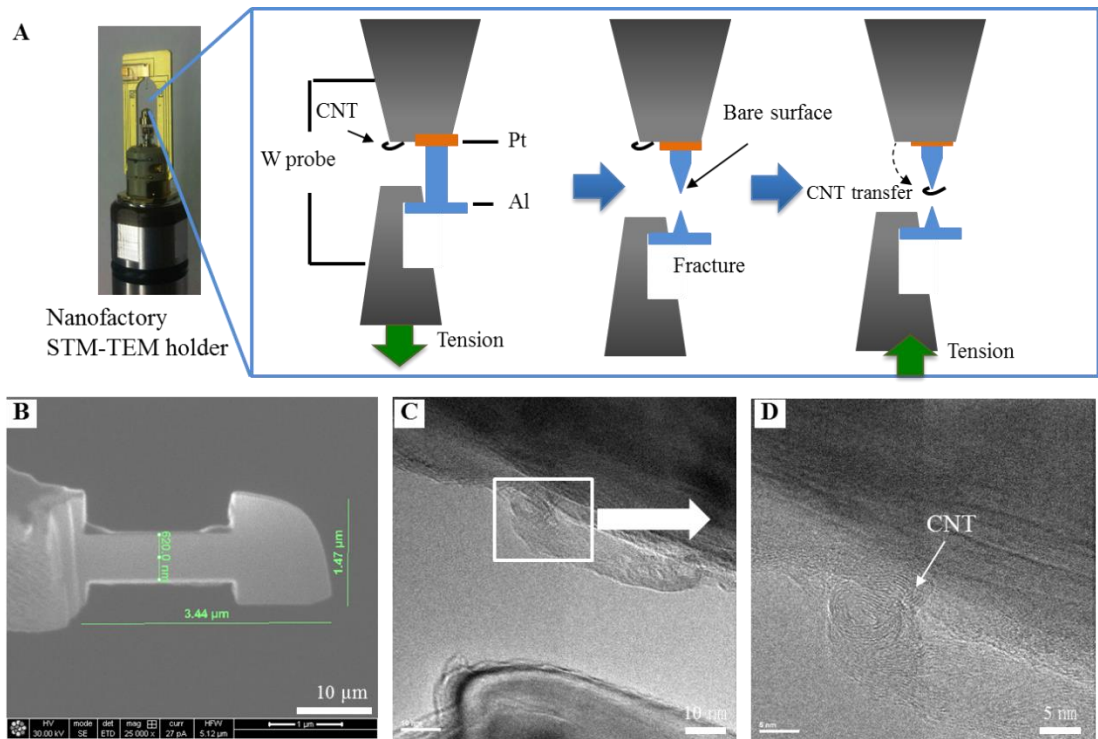


**Fig. S8 Fabrication process of the oxide-free Al and transferring CNT onto the surface.** (A) nanofactory holder and schematic diagram for preparing of the oxide-free Al and CNT transfer process. (B) SEM image after FIB. (C) TEM image after CNT transfer and (D) high-resolution TEM of the CNT wall.

For the comparison purpose, we pulled out the Al sample in the air to oxidize the surface. The CNT was transferred to the oxide passivated Al surface (Fig. S9A).

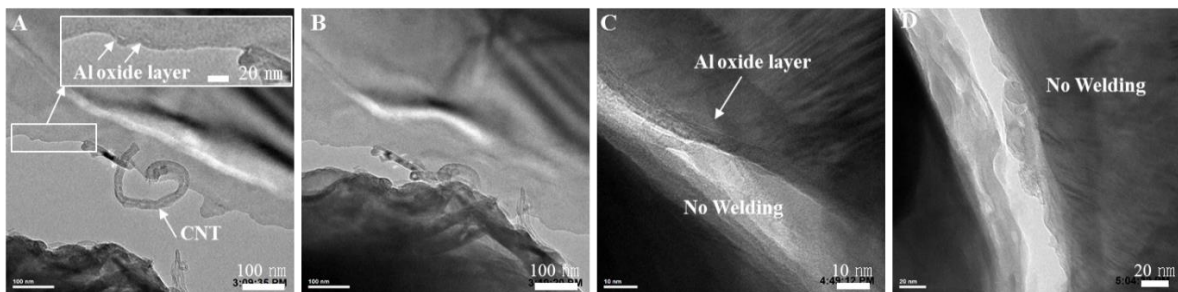


**Fig. S9 Non-cold welding of the oxide layer-coated Al.** (A) CNT on oxide coated-Al surface. (B) Contacting of two Als. The surface between two Als after (C) shearing and (D) impact.

When we contact the two Al, no atomically surface-diffusion binding between Al-Al was observed in the presence of the surface oxide as shown Fig. S9B and C. Therefore, the subsequent CNT embedding did not occur in the oxide formed Al (see Movie S4).

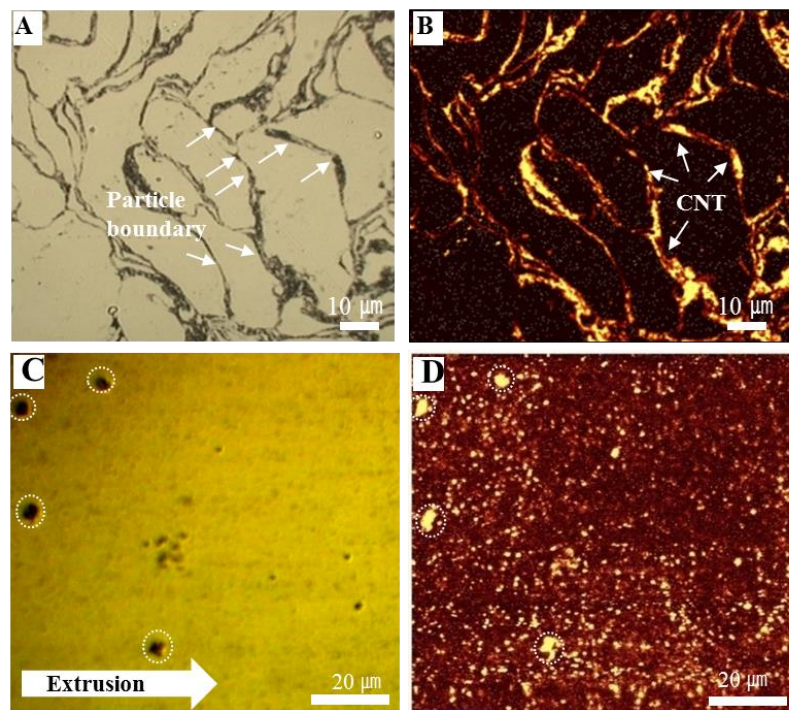


**Fig. S10 Comparison of the dispersion of CNT after Al+CNT composite fabrication in oxidation/non-oxidation condition.** (A) Optical image and (B) G band mapping in confocal Raman spectra at the oxidation condition. (C) Optical image and (D) G band mapping in confocal Raman spectra at the non-oxidation condition.

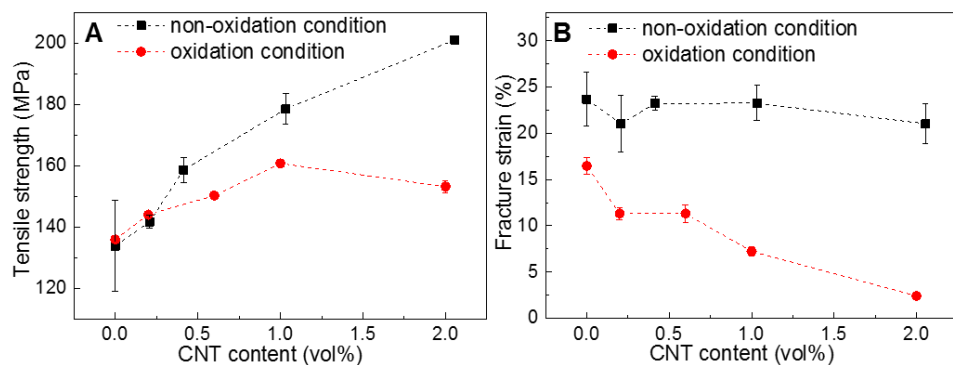


**Fig. S11 The mechanical properties under different ambient conditions.** A comparison of the mechanical properties with clustered CNTs: (A) tensile strength and (B) fracture strain as a function of the CNT concentration.

### E. Atomistic diffusivity

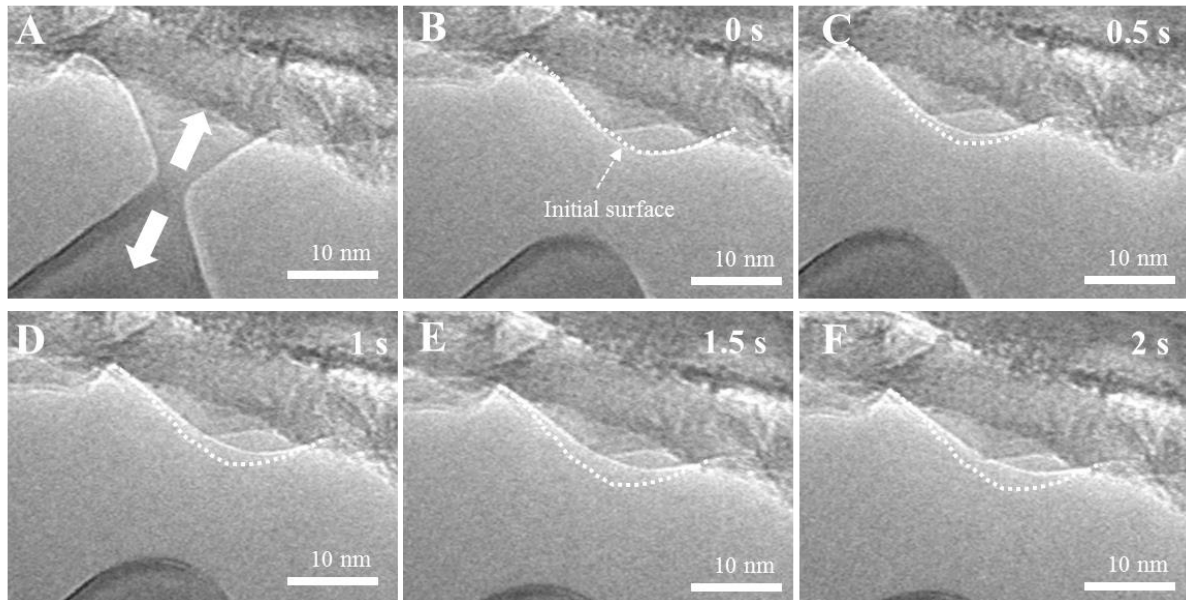


**Fig. S12 flattening of the surface analysis after the massive atomic cluster transfer on the top of the CNT in in-situ TEM.** (A) transferring of the Al, (B) 0s, (C) 0.5s, (D) 1s, (E) 1.5s and (F) 2s. white dot indicates the original surface of the Al.

The quantitative analysis of the surface diffusivity in in-situ TEM observation can be obtained by taking flattening time of a single-hump wrinkled surface after coverage of CNT via cold welding in Fig. S12. The surface diffusivity  $D_s$  can be estimated by the following equation.<sup>5</sup>

$$D_s = -\frac{Sk_B T}{v\gamma_M \Omega^2} \left(\frac{\lambda}{2\pi}\right)^4$$

Where  $S$  is the slope from the natural logarithm of height vs a linear function of time in Fig. S4A.  $\Omega$  is atomic volume ( $0.0166 \text{ nm}^3/\text{atom}$ ),  $T$  is room temperature (298 K),  $v$  is the surface atomic density ( $v_{(111)}=0.1 \text{ atom}/\text{nm}^2$ ), and  $\lambda$  is the segment length in the rest position (24 nm in Fig. S13)

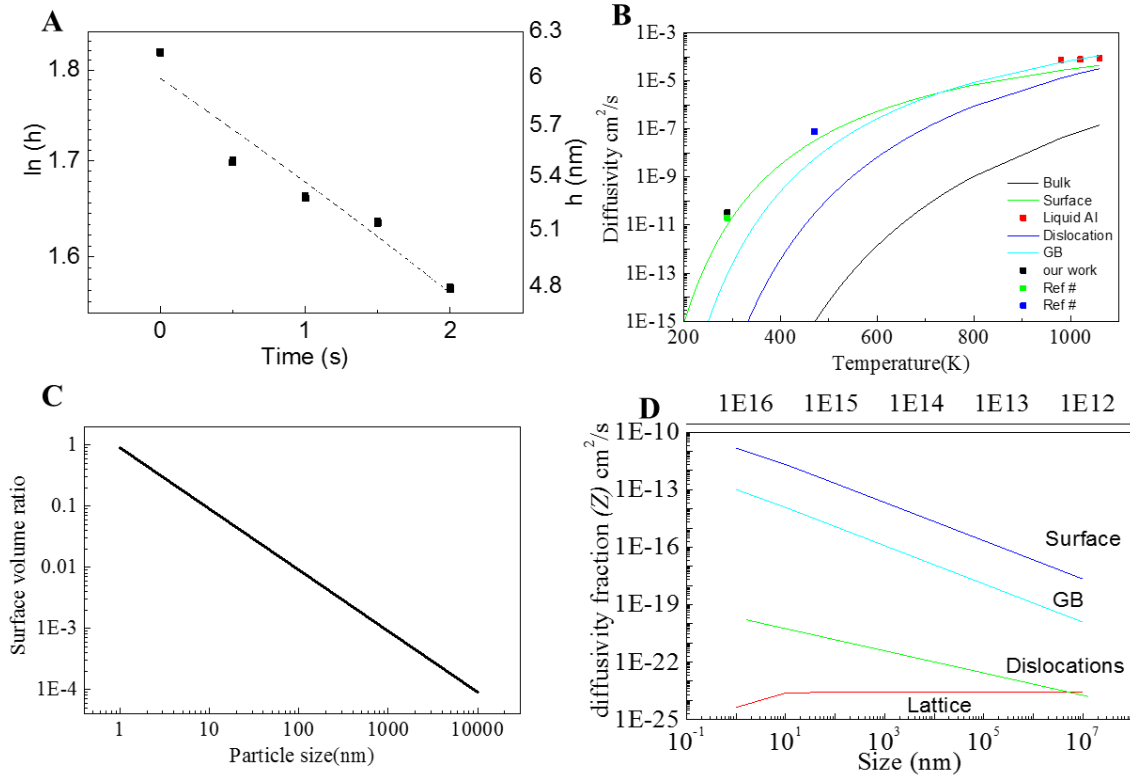


**Fig. S13** (A) The measured retreating distance  $h$  on the surface CNT versus exposure time, (B) self-diffusivity of the atoms in Al versus temperature. (C) volume fraction of the surface to bulk volume ( $\text{nm}^3/\text{nm}^3$ ). (D) Effective self-diffusivity of the Al atoms depending on the size according to the area fraction of surface, GB, dislocation. at room temperature.

Diffusivity of Al is extracted from the existing literature value. All the diffusion coefficient satisfy Arrhenius equation.

$$D = D_0 \exp\left(-\frac{E_a}{k_B T}\right)$$

Where  $D_0$  is the pre-exponential factor,  $E_a$  is the activation energy, and  $k_B$  is the Boltzmann constant. The activation energy and pre-exponential factor were obtained from previous reported empirical value in Table S2.<sup>6</sup> The diffusivity of the surface, GB, dislocation, and bulk are plotted according to temperature change in Fig. S13B.

The ratio of surface volume fraction ( $V_s$ ) to the bulk volume ( $V_b$ ) was calculated by following equation.

$$\frac{V_s}{V_b} = \frac{t3\pi r^2}{\frac{4}{3}\pi r^3}$$

Where  $r$  is the diameter of particles and  $t$  is the thickness of top most surface ( $\sim 0.3$  nm). The ratio  $V_s/V_b$  is plotted in Fig. S13C

We have calculated the contribution of the diffusivity fraction ( $Z$ ) in the entire system.

$$Z = Df$$

Where  $D$  is the original diffusivity of the surface, GB, dislocation, and bulk,  $f$  is the area fraction of its compound.  $t$  for GB was consider to be 0.3 nm.  $Z$  is plotted in Fig. S13B

Therefore, the effective diffusivity can be introduced from the sum of all the diffusivity component.

$$D_{Eff.} = Z_s + Z_{GB} + Z_{disl.} + Z_L$$

Table S3. Activation energy and diffusivity of Al<sup>6</sup>

Type	$E_a$ (kcal/mol·K)	$D_o$ (cm <sup>2</sup> /s)	$D$ at 298K(RT) (cm <sup>2</sup> /s)	Fraction ( $f$ ) at 10nm	$Z$ (cm <sup>2</sup> /s)
Surface	12.1	0.014	1.8E-11	0.1164	2.1E-12
GB	16.6	0.3	2.0E-13	0.0591	1.2E-14
Dislocation	23.3	2.1	1.6E-17	1E-3	1.6E-21
Bulk	32	0.5	2.7E-24	0.823	2.4E-24

## B. Measurements

### Microstructure characterization

The microstructure of the Al+CNT composites was characterized by FESEM and high-resolution TEM (HRTEM, 200 keV, 2100F, JEOL, Japan). The specimen for microstructure observation was prepared by a mechanical polishing (MetPrep3TM/PH-3TM, ALLIED, USA).

SiC paper (400~1200 grit) and alumina (3  $\mu\text{m}$  and 1  $\mu\text{m}$ ) and silica (0.04  $\mu\text{m}$ ) suspensions were used to polish the specimen. The TEM sample was prepared using focused ion beam (FIB, SMI3050TB, SII, Japan) with a Ga ion milling process and a Pt protection layer. Elemental analysis was performed with energy-dispersive X-ray spectroscopy (EDS). The crystallographic analysis was performed using X-ray diffraction (XRD, Cu K $\alpha$ , 1.54  $\text{\AA}$ , D/MAX 2500, Rigaku, Japan) and electron-backscattered diffraction (EBSD, EDAX). The EBSD patterns were selectively collected from orientation angles greater than 15°. The CNT distribution in the Al matrix was characterized using confocal Raman spectroscopy (CRM 200, Witech, German).

### **Mechanical properties measurement**

The mechanical properties were characterized using an ultimate tensile tester (Landmark 25 kN, MTS, USA) and a micro-Vickers hardness tester (HM-211, Mitutoyo, Japan). The tensile specimen was prepared using a mechanical mill with a 6 mm gage diameter and a gage length of 25 mm (E8/E 8M-08, ASTM). The tension test was performed at a speed of 2 mm/min. The hardness test was performed on a cross-section of the specimen using a load of 100 g for 10 s.

### **Characterization of interfacial Al-C bonding**

The interfacial Al-C bonds were characterized by XRD, Raman and XPS. The  $\text{Al}_4\text{C}_3$  peaks in the XRD patterns were clearly visible with SPS processing at temperatures greater than 300 °C

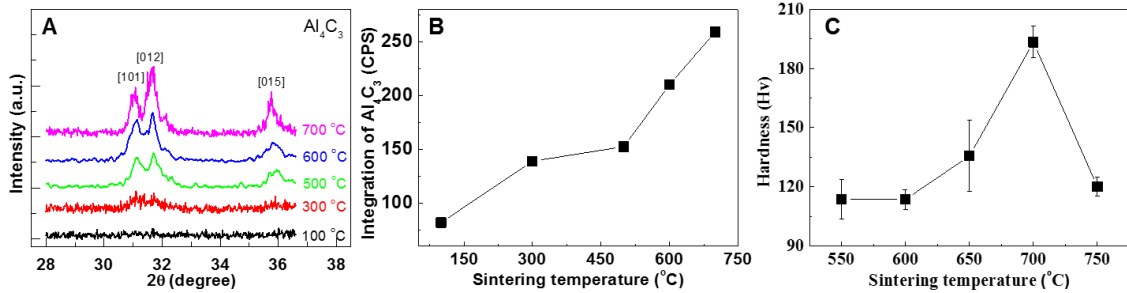


(Fig. S14A and B). The amount of the  $\text{Al}_4\text{C}_3$  phase is proportional to the hardness of the composite (Fig. S14C). The increase of the hardness as a function of  $\text{Al}_4\text{C}_3$  phase indicates the role of the interfacial Al-C covalent bonds for load transfer. The blueshift of the G-band peak position in the Raman spectra provides further evidence of the presence of Al-C covalent bonds in the composite<sup>12</sup>, which is additionally supported by the C1s peak in the XPS spectrum (Fig. S15A and B). The frequently observed broken CNTs at fracture area are another evidence of the sufficient interfacial bonding.

**Fig. S14** (A)XRD data for the samples in terms of the SPS temperature used to detect  $\text{Al}_4\text{C}_3$  formation. (B) The formation of  $\text{Al}_4\text{C}_3$  integrated by XRD and (C) the hardness of the Al+ 10 wt% CNT composite as a function of the sintering temperature. The formation of  $\text{Al}_4\text{C}_3$  indicates strong interfacial strength between Al and CNT. Although the interfacial strength monotonically increased up to 700 °C with increasing sintering temperature, the hardness was degraded at high temperature (750 °C) due to CNT disintegration.

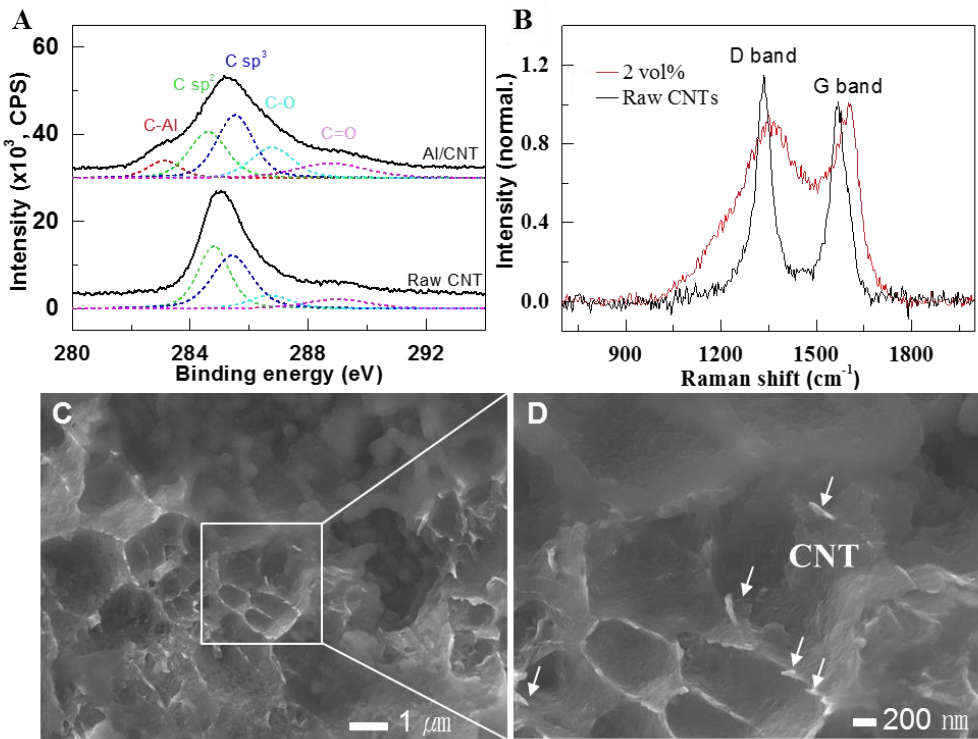


**Fig. S15 Al-C interfacial covalent bonds.** (A) XPS for C1s. The binding energy for carbon determined from the XPS spectrum of the Al/CNT 10 wt% composite after SPS process. A large volume percentage was used for the XPS measurements to clearly show the carbon peaks. (B) Raman spectra of raw CNT and 2vol% CNT in Al. The upshift of G band indicates charge transfer from CNT to Al through Al-C covalent bonds. SEM images of the fractured area after tension testing. (C) The Al/CNT 2 vol% composite and (D) protruding CNTs indicated by arrows, indicating efficient load transfer from the strong anchoring of Al to the CNT surface.

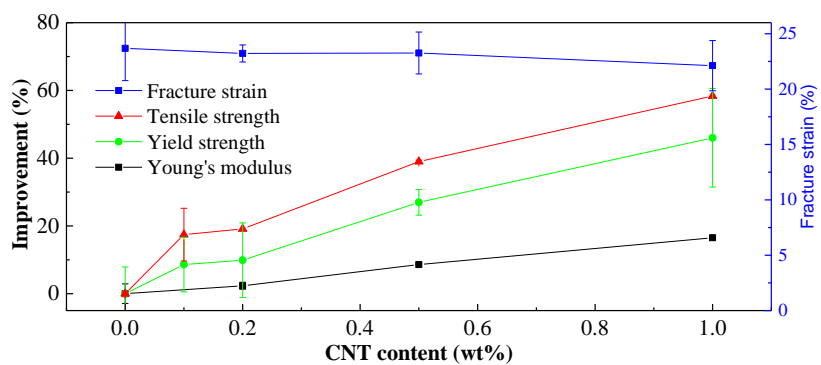


**Fig. S16 Fracture strain and Relative improvement of Young's modulus, tensile strength and yield strength.**

### The specific strengthening efficiency (R)

The specific strengthening efficiency (R),  $R = \frac{\sigma_c - \sigma_m}{v_c \sigma_m}$ , where  $\sigma_c$  and  $\sigma_m$  are the tensile strengths of the composite and matrix, respectively, and  $v_c$  is the volume percentage of CNTs to metal, is the relative tensile strength normalized by the CNTs vol% (Fig. S17A). The strengthening efficiency is generally low at high CNT content due to the limited dispersion ability. The specific strengthening efficiency (R) versus fracture strain curve clearly shows distinctive behavior at a CNT content of 2 vol%. The right region (with less than 2 vol% CNTs) shows samples with high fracture strain and high specific strengthening efficiency. In this region, the CNTs are well dispersed so that the number of Al-C bonds increases further and the dislocation propagation is effectively pinned, as shown in the right inset of Fig. S17B. However, in the left region (with more than 2 vol% CNT), both the fracture strain and the specific strengthening efficiency are substantially reduced. This trend is also well correlated with mechanical properties, such as the tensile strength and the Vickers hardness, for different CNT contents. Although SPS process produces interfacial Al-C bonds, the agglomerated CNTs provide less number of Al-C bonds due to the low interfacial area between Al and CNTs, resulting in inefficient dispersion hardening. The CNTs agglomeration at higher content eventually resulted in poor specific mechanical strength and fracture strain.

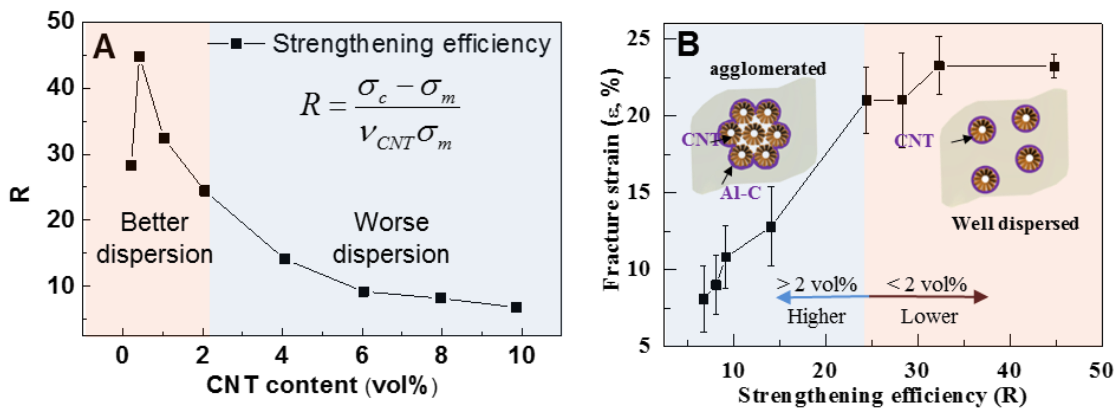


**Fig. S17** (A) The fracture strain versus strengthening efficiency. Two distinct regions are clearly visible. The inset shows a schematic of degree of CNT dispersion.

### Processing factors for affecting the specific toughness, specific strengthening efficiency, and specific fracture strain.

The toughness, ( $\int_0^{\varepsilon_f} \sigma d\varepsilon$ ), is defined as a tolerance energy of absorbing external stress before a final fracture from the strain and stress curve. The toughness with respect to pure Al increases as the CNT content approaches to 2 vol% (Fig. 4). Our process provides greater toughness than previous wet processes.<sup>7</sup> This result implies that maintaining inert conditions by preventing Al oxidation to induce surface welding during mechanical pulverization is critical. At higher CNTs content (greater than 2 vol%(1wt%)), the toughness gradually decreases until a value that is worse than that of pure Al. These results suggest that, in spite of enhanced mechanical properties by the incorporated CNTs, the agglomeration of CNTs significantly gives harmful effects for the ductility by provoking crack initiation.

Figure 5 summarizes the relationship of these properties with the material processing methods for the existing experimental data. As examples, the slurry mixing method caused the formation of a strong oxide layer on the surfaces of the Al particles, which resulted in poor CNTs dispersion, causing the low load transfer, the poor dislocation interactions with the CNTs, and the pore generations from the CNTs clusters.<sup>8</sup> Therefore, low strengthening efficiency, low toughness, and low fracture strain were obtained. In comparison, the low-energy ball milling (LEBM) process imparted mechanical impacts to the CNTs and provided the better CNTs dispersion than the solution processing.<sup>9</sup> Although this better dispersion results in an improved toughness as a consequence of maintaining the fracture strain, a low strengthening efficiency is observed due to the low load transfer from the poor interface. Strong interfacial bonding can be accommodated by *in-situ* CNTs growth on Al and improves load transfer, resulting in the greater strengthening efficiency without the loss of toughness and fracture strain.<sup>10</sup> High-energy ball milling (HEBM) generates highly dispersed CNTs and Al–C covalent bonds from the strong mechanical impact, improving the strengthening efficiency.<sup>11,12</sup> However, the structural damage of the CNTs cannot be avoided from the strong mechanical impact, and consequently, the poor

quality CNTs structure give a low specific toughness and fracture strain due to the inefficient pinning of dislocation propagation. The combination of ultrasonication and ball milling provides the better dispersion and a strong interface from the chemical functionalization without damage to the CNTs walls.<sup>7,13-15</sup> Therefore, the strengthening efficiency showed higher values than those achieved with LEBM. Nevertheless, the oxygen-containing solvent caused the oxidation of Al particles during the ultrasonication process, which rendered this method relatively inefficient with respect to the dispersion of CNTs into the Al grains. This again induced poor interaction between the CNTs and dislocations, which resulted in the low fracture strain. Our cold-welding induced mechanical dispersion of CNTs along with a strong interface yields a high degree of CNTs dispersion, even inside the Al grains, while minimizing the damage to the CNTs. Our method, therefore, provides not only high values of the strengthening efficiency and specific toughness but also a high specific fracture strain.

**Movie S1** <http://li.mit.edu/S/KangPyoSo/Upload/microwavetreatment.wmv>

**Movie S2** <http://li.mit.edu/S/KangPyoSo/Upload/meltingprocess.mpg>

**Movie S3** <http://li.mit.edu/S/KangPyoSo/Upload/Movie1non-oxidewelding.wmv>

**Movie S4** <http://li.mit.edu/S/KangPyoSo/Upload/MovieS1-oxidewelding.wmv>

## References

- 1 So, K. P. *et al.* SiC formation on carbon nanotube surface for improving wettability with aluminum. *Compos Sci Technol* **74**, 6-13 (2013).
- 2 Y. H. Lee, K. P. S., H. K. Park, E. S. Kim. Method for increasing electro conductivity of aluminum using carbon nanotube and the material. Korea patent 10-1114628 (2012).
- 3 Xie, G. Q. *et al.* Effect of interface behavior between particles on properties of pure Al powder compacts by spark plasma sintering. *Mater Trans* **42**, 1846-1849, doi:DOI 10.2320/matertrans.42.1846 (2001).

- 4 Munir, Z. A., Anselmi-Tamburini, U. & Ohyanagi, M. The effect of electric field and pressure on the synthesis and consolidation of materials: A review of the spark plasma sintering method. *J Mater Sci* **41**, 763-777, doi:10.1007/s10853-006-6555-2 (2006).
- 5 Xie, D.-G. *et al.* In situ study of the initiation of hydrogen bubbles at the aluminium metal/oxide interface. *Nat Mater* **14**, 899 (2015).
- 6 Tan, C. M. & Roy, A. Electromigration in ULSI interconnects. *Materials Science and Engineering: R: Reports* **58**, 1-75 (2007).
- 7 Jiang, L., Li, Z. Q., Fan, G. L., Cao, L. L. & Zhang, D. The use of flake powder metallurgy to produce carbon nanotube (CNT)/aluminum composites with a homogenous CNT distribution. *Carbon* **50**, 1993-1998, doi:10.1016/j.carbon.2011.12.057 (2012).
- 8 Wu, J., Zhang, H., Zhang, Y. & Wang, X. Mechanical and thermal properties of carbon nanotube/aluminum composites consolidated by spark plasma sintering. *Materials & Design* **41**, 344-348 (2012).
- 9 Esawi, A. M. K., Morsi, K., Sayed, A., Gawad, A. A. & Borah, P. Fabrication and properties of dispersed carbon nanotube-aluminum composites. *Mat Sci Eng a-Struct* **508**, 167-173, doi:10.1016/j.msea.2009.01.002 (2009).
- 10 He, C. N., Zhao, N. Q., Shi, C. S. & Song, S. Z. Mechanical properties and microstructures of carbon nanotube-reinforced Al matrix composite fabricated by in situ chemical vapor deposition. *J Alloy Compd* **487**, 258-262, doi:10.1016/j.jallcom.2009.07.099 (2009).
- 11 Choi, H. J., Shin, J. H. & Bae, D. H. Grain size effect on the strengthening behavior of aluminum-based composites containing multi-walled carbon nanotubes. *Compos Sci Technol* **71**, 1699-1705, doi:10.1016/j.compscitech.2011.07.013 (2011).
- 12 So, K. P. *et al.* Low-temperature solid-state dissolution of carbon atoms into aluminum nanoparticles. *Scripta Mater* **66**, 21-24, doi:10.1016/j.scriptamat.2011.09.031 (2012).
- 13 Deng, C. F., Wang, D. Z., Zhang, X. X. & Li, A. B. Processing and properties of carbon nanotubes reinforced aluminum composites. *Mat Sci Eng a-Struct* **444**, 138-145, doi:10.1016/j.msea.2006.08.057 (2007).
- 14 Jiang, L., Li, Z. Q., Fan, G. L., Cao, L. L. & Zhang, D. Strong and ductile carbon nanotube/aluminum bulk nanolaminated composites with two-dimensional alignment of carbon nanotubes. *Scripta Mater* **66**, 331-334, doi:10.1016/j.scriptamat.2011.11.023 (2012).
- 15 Nam, D. H. *et al.* Synergistic strengthening by load transfer mechanism and grain refinement of CNT/Al-Cu composites. *Carbon* **50**, 2417-2423, doi:10.1016/j.carbon.2012.01.058 (2012).